Energy

FOSSIL

DOE/SF/11564-6
(DE84012410)

FLOW OF FOAM THROUGH POROUS MEDIA

By
Owete S. Owete
William E. Brigham

Work Performed Under Contract No. AC03-81SF11564

Stanford University Petroleum Research Institute
Stanford, California

Technical Information Center
Office of Scientific and Technical Information
United States Department of Energy

DISCLAIMER

This report has been reproduced directly from the best available copy.

Available from the National Technical Information Service, U. S. Department of Commerce, Springfield, Virginia 22161.

Price: Printed Copy A06
Microfiche A01

Codes are used for pricing all publications. The code is determined by the number of pages in the publication. Information pertaining to the pricing codes can be found in the current issues of the following publications, which are generally available in most libraries: *Energy Research Abstracts (ERA); Government Reports Announcements* and Index (*GRA* and I); *Scientific and Technical Abstract Reports (STAR);* and publication NTIS-PR-360 available from NTIS at the above address.

Printed in the United States of America
USDOE Technical Information Center, Oak Ridge, Tennessee

DOE/SF/11564-6
(DE84012410)
Distribution Category UC-92a

FLOW OF FOAM THROUGH POROUS MEDIA

SUPRI TR-37

By

Owete S. Owete
William E. Brigham

W. E. Brigham, Principal Investigator
Stanford University Petroleum Research Institute
Stanford, California 94305

H. J. Lechtenberg, Technical Project Officer
San Francisco Operations Office
Fossil, Geothermal and Solar Division
1333 Broadway
Oakland, California 94612

Work Performed for the Department of Energy
Under Contract No. DE-AC03-81SF11564

ACKNOWLEDGEMENTS

Financial support during the course of this work was provided by the Department of Energy through the Stanford University Petroleum Research Institute, under Contract No. DE-AC03-81SF11564.

ABSTRACT

This study focuses on the pore level behavior of foam in porous media. Air was injected into porous micromodels which had previously been filled with an aqueous solution of surfactant. The micromodels consist of an etched silicon wafer anodically bonded to a glass plate. The model simulates a monolayer of porous matrix. Three homogenous models of different pore dimensions and one heterogeneous model were used. Visual observations were made to determine the flow characteristics of "foam" under varying air injection rates, pore dimensions and surfactant concentration. Foam flow mechanisms, as observed in the micromodels, were recorded on video tapes. These tapes are available at the Stanford University Petroleum Research Institute, Stanford, California.

The observed mechanisms can be broadly classified into two: membrane and foam bubble propagation. Propagation of membranes, air-liquid interfaces, occurred in the homogeneous porous media at both low and high surfactant concentrations, and in the heterogeneous model at low surfactant concentration. Foam bubble propagation occurred only in the heterogeneous model at high surfactant concentrations.

In the homogeneous micromodels, the wetting phase (surfactant solution) formed a continuous liquid network around the matrix. The air was found to propagate as tubular bubbles moving and extending over several pores. The flow mechanism was only slightly affected when different air injection rates, pore dimensions and surfactant concentrations were used.

Foam was found to be generated in the heterogeneous model. Air and liquid were propagated by a combination of channel flow (with liquid confined to small pores) and a bubble "break and reform" process. The break and reform process was caused by snap-off actions at pore constrictions.

A considerable reduction of effective mobility was observed in the presence of foam, compared to air-water systems without surfactant. Effective air mobility decreased with an increase in surfactant concentration in both the homogeneous and heterogeneous porous media. At a specific concentration, below the critical micelle concentration, mobility reduction converged to one value regardless of concentration changes. In the heterogeneous porous medium, surfactant concentration affected the flow mechanism. Foam bubbles produced at high surfactant concentrations were smaller than those generated at low surfactant concentrations.

TABLE OF CONTENTS

LIST OF TABLES

LIST OF FIGURES

1. INTRODUCTION

Foam has been used in the petroleum industry for various operations such as drilling, completion, fracturing, acidizing, workover and mobility control during thermal oil recovery. One technique for thermal oil recovery is the injection of steam into a reservoir to reduce oil viscosity and make the oil more mobile.

Because of the density difference between steam and oil, the lighter steam tends to flow on top and "ride" over the oil. This preferential movement of steam through the upper part of the reservoir, termed gravity override, reduces the amount of reservoir rock contacted by steam. Steam also channels through the more permeable zones of the reservoir. As a consequence of channeling and gravity override, the distribution of heat through the reservoir is not uniform and this leads to early steam breakthrough in production wells and reduces oil recovery.

Foam has been suggested as a "blocking" agent in steam injection to reduce gravity override and steam channeling. The reason is that foam may reduce the mobility of steam and this reduction is proportionately higher in the more permeable sands. Thus, the success of a steam-foam project will depend on knowledge of the mechanism of foam flow through the interstices of the porous medium, and how well this knowledge is used to tailor the design to reservoir conditions.

Many studies have identified factors influencing the flow behavior of foam in porous media. Most of these studies were concerned with macroscopic flow. A more meaningful approach could be to study the general flow behavior at the pore level, and then relate the results to macroscopic experiments and field operations.

Foam can be generated by simultaneously injecting both gas and liquid into a porous medium. In this study, however, foam was generated by injecting air into micromodels that had previously been saturated with an aqueous solution of surfactant. Micromodels of differing pore dimensions were used. A visual study was made of foam generation and propagation in these models. The effects of air injection rate and foamer concentration on the air mobility and the flow behavior of the foam were investigated.

Before starting this experiment, a review was made of previous studies on foam flow in porous media and the types of physical micromodels used by researchers to study fluid flow in porous media (petroleum reservoirs). This review or literature survey is given in the following section.

2. LITERATURE SURVEY

A review of foam research and applications of foam in the petroleum industry was compiled by Marsden (1979). Consequently, this literature survey will focus primarily on the mechanism of foam flow in porous media. In addition to the flow of foam in porous media, an understanding and knowledge of micromodels that has been used by other researchers was needed to design the experiments. A brief discussion of the papers describing micromodels is provided.

2.1 MECHANISM OF FOAM FLOW IN POROUS MEDIA

Although the general flow behavior of foam is the subject of this study, two subjects are of particular importance: (1) the propagation of foam and its components in porous media, and (2) the mobility of gas in the presence of foam. Snap-off in water-wet pores will also be discussed since the phenomenon produces air-liquid interfaces. Foam is a dispersion of air in liquid characterized by a network of air-liquid interfaces.

2.1.1 Propagation of Foam in Porous Media

Marsden and Khan (1966), Raza and Marsden (1967), David and Marsden (1969), Holcomb, et al. (Nov. 1980), and Holbrook, et al. (1981), have studied the rheology of foam to gain insight into its flow behavior. There is a general agreement that foam behaves like a pseudoplastic fluid with high apparent viscosity. There are diverse opinions, however, on how foam and its components are transported through the network of pores.

In petroleum reservoirs, fluids are generally considered to exhibit pore channel flow, wherein permeability is a function of saturation only. If foam flowed as in channel flow, its components would move independently and flow through separate and different pore channels. Holm (1968) contends that foam continously separates into gas and liquid in the porous medium and continually reforms foam. The work of Marsden and Khan (1966), Bernard and Holm (1964) and Raza (1970) indicates, however, that the permeability of foam is not a single function of saturation. This implies that foam does not exhibit pore channel flow.

Researchers such as Fried (1961), Marsden and Khan (1966), Raza and Marsden (1967) and David and Marsden(1969) proposed the homogeneous fluid flow mechanism. Foam is considered to be a continuum; the gas and liquid flow at the same rate, and the foam behaves as a single fluid with high apparent viscosity. Gas permeability reduction is achieved by a plug-type flow. Because the injectivity of foam did not match that of a high viscosity oil, Raza (1970) concluded that foam flow behavior in a porous medium cannot be described merely in terms of a single high viscosity fluid. Based on quality/viscosity measurements of flowing and bulk foams, Minssieux (1974) concluded that foam did not flow as single fluid. He suggested, however, that foam flow can be interpreted using the concept of foam quality as applied to the whole fluid. Foam quality is the ratio of gas volume to the total volume (gas and liquid) of the foam. Despite the differences in these and other experimental findings, it is generally agreed among researchers that a low quality foam can and does flow as a single fluid: bubbles are stable, fairly uniform, and small enough to pass through the pore constrictions without breaking.

Foam with large and less stable bubbles is less likely to flow as a single fluid. From visual studies, Fried (1961), Holm (1968) and Mast (1972) deduced that foam is propagated inside a porous medium by the breaking and reforming of foam bubbles. The gas flows as a discontinous phase (intermittent gas flow) while the liquid is transported as a free phase via the film network. Other work by Bernard and Holm (1964), Marsden and Khan (1966) and Nahid (1971) suggests that the liquid flows according to Darcy's law. Nahid (1971) proposed that the gas flow could be treated according to Darcy's law if a correction factor for the gas permeability is used.

The last of the mechanisms proposed to explain how foam is propagated in porous media states that a large portion of the gas is trapped in the porous medium. The liquid and the remaining gas, according to Kolb (1964), flow according to Darcy's law. Mast (1972) noted that as the porous system became filled with foam, some channels were blocked and flow took place through only a part of the model. From gas tracer studies, Nahid(1971) showed the existence of an immobile gas saturation which increased with the concentration of the surfactant (foamer solution) used. The immobile gas saturation ranged from only 4% in the absence of a surfactant up to 30% at a surfactant concentration of 1%.

From the observations made in most of the work cited, some insight can be obtained on how foam may impede the flow of gas. The mobility of gas in the presence of foam has been studied in some detail by previous researchers.

2.1.2 Gas Mobility in the Presence of Foam

Holm (1968) and Albrecht and Marsden (1970) showed that foam impedes the flow of gas in porous media. This reduction in gas mobility, as indicated by Bernard and Holm (1964), is greater for higher permeability sands. Raza (1970) showed that high quality foams (large bubbles) were produced in the high permeability sands which contain uniformly distributed large pores. Mast (1972) discussed the importance of pore geometry in the process of bubble formation and the size of the bubbles: a network of small pores adjoined by larger pores facilitates bubble formation. Such a network offers sites of regeneration in a porous medium. Mast extended Gardescu's work (1930) to obtain equations relating minimum bubble radius with pore dimensions and interfacial properties of the liquid. The work of Deming (1964) indicates a possible effect of pore structure on foam flow behavior.

The effect of foamer concentration on the nature and type of foam produced in porous media has been studied in some detail by Holm (1968), David and Marsden (1969), Raza (1970), Mast (1972) and Kander and Schechter (1976). Foamer concentration affects the quality of the foam and the size and nature of the foam bubbles that are produced. The average foam bubble diameter is proportional to foam quality, which increases with concentration. Marsden, et al. (1977) observed that the discrepancy between results obtained in different laboratories may have been due to researchers using different foamer concentrations. Fine textured foams are obtained with concentrated foamer solutions, and coarse foams are obtained with dilute foamer solutions. Mast (1972) observed that high concentrations of foaming agents produced more stable foams whose bubbles could be displaced from large pores into smaller

ones without breaking. The work by Holcomb et al. (1981) indicates that the mobility to gas in the presence of foam decreases with surfactant concentration. However, beyond the critical micelle concentration (CMC), no further decrease in gas mobility was noticed. Gas mobility was not measured directly; the pressure drop and apparent viscosity were measured for different concentration systems.

The effect of flow rate (gas or liquid) on foam flow behavior has not been extensively studied. Bikerman (1973) has reviewed various work involving static columns of foam. When gas was bubbled through a surfactant solution, the height of the static column of foam generated was shown to be directly proportional to the gas flow rate. This effect on static foam can be related to flowing foam since the behavior of the latter is affected by bubble texture and size. Raza (1970) injected gas and surfactant solution simultaneously into unconsolidated sand packs. The steady state saturations were found to be constant and independent of the fluid flow rates. On the other hand, the effective permeability to gas and water (surfactant solution) changed with a change in the volumetric flow rate. Raza's work suggests some direct influence of fluid flow rate on the effective permeability to gas in the presence of foam. A survey of the flow rates used by previous reseachers is shown in Table 2.1. The simultaneous injection of gas and surfactant solution into a porous medium is one of the two methods commonly used to produce foam in situ.

The second method of generating foam in situ is to inject air or gas into a porous medium saturated with an aqueous surfactant solution. For a water-wet porous medium, the process can be described as the displacement of a wetting phase by a nonwetting phase. During

Table 2.1

A SURVEY OF FLOW RATES USED IN FOAM EXPERIMENTS

AUTHORS (Reference)	POROUS MEDIA				FLOW VELOCITY $q/A\phi$ (ft/D)		REMARKS
	Type	K_a (darcys)	ϕ (%)	A (cm^2)	Liquid	Gas	
Holm, L. W. (1968)	U	5	40	11.4	1.2	6.2	External foam generation (75% Γ)
Bernard, G. G. & Holm, L. W. (1964)	U	125	40		10*		In-situ foam generation**
	C	3.9	20		100*		
Minssieux, L. (1974)	U glass beads	4.5	40 (?)	0.95	200	5000	In-situ foam generation (80-90% Γ)**
	C	2.2	21	1.99	100	700	(50-90% Γ)
Raza (1970)	U	3	40	116	1.5	1	In-situ foam generation**
Mahmood (1981)	U	14.5	40	19		400	In-situ foam generation

U - Unconsolidated

C - Consolidated

*Not sure if "porosity" is included in velocity term.

**Simultaneous injection of liquid and gas.

this displacement, a phenomenon called "snap-off" often occurs. This phenomenon is discussed next.

2.1.3 Snap-Off in Water-Wet Pores

Roof (1970) investigated the conditions that must be met in order that the oil emerging from a water-wet constriction will separate (choke-off, snap-off or pinch-off) into a droplet in a larger channel. Such flow of water and oil in a water-wet system is similar to the displacement of an aqueous surfactant solution by air in a water-wet porous medium. If snap-off occurs in the latter case, separate air bubbles and a network of air-liquid interfaces will be produced.

For a capillary controlled displacement, the leading spherical interface becomes unstable if its capillary pressure is less than the capillary pressure at the throat. Roof considered toric pores and computed the equilibrium location of the leading front as a function of tore radius. The front (head meniscus) is always at least seven pore radii from the throat of the constriction before snap-off (choke-off) can occur. He made an experimental verification of the theoretical analysis. His experimental observations show that irregularity in the pore seems to be necessary for a snap-off process to occur within reasonable periods of time.

Mohanty, et al. (1980) made an energy stability analysis of neck and head menisci. They determined the minimum ratio of pore body radius to adjacent throat radius (r_b/r_t) required for snap-off to occur. For most shapes considered, snap-off occurs when this ratio is greater than three.

In both Roof's and Mohanty's work, the criteria for snap-off are

independent of interfacial tension and other fluid properties. For a snap-off to occur in a flow channel, the leading fluid interface must advance into cavities considerably larger than pore throats. The relative size of pores and throats, rather than their absolute sizes, thus influence choke-off.

Wardlaw and Cassan (1979) commenting on the effect of pore structure recovery efficiency contend that "In regular packings of equal spheres (cubic, rhombohedral-hexagonal), no capillary trapping can be expected because a nonwetting phase entering and filling a pore will be constrained by the pore wall on the downstream side before the curvature can expand enough to cause snap-off at the upstream pore-neck."

Through the rest of this report, "snap-off" will be used in preference to the terms "choke-off" and "pinch-off".

Having reviewed some of the flow processes that could take place in this experiment, it remains to find a suitable physical model of a petroleum reservoir porous medium. The primary objective of this work, a visual study of the pore level behavior of foam, limits one to the use of micromodels. The following section describes the micromodels used by previous researchers to study flow behavior in porous media.

2.2 MICROMODELS

Micromodels permit a pore-size level study of a fluid flow process. Simple micromodels, capillary tubes, were used by Marsden and Khan (1966) and David and Marsden (1969) to study the rheology of foam. The single layer glass bead model is a closer representation of a porous medium. This was used by Sharma (1965) to study the foam drive process, and Egbogah and Dawe (1980) to study the size distribution of

oil droplets.

Mattax and Kyte (1961) used a network of etched capillaries to study fluid distributions under various wettability conditions. In this method, interconnecting capillary grooves were etched into a flat glass plate. A second glass plate was fused to the etched plate. Inlet and outlet ports were made by drilling holes into the unetched plate. The etching technique consisted of coating a glass plate with wax, scribing lines through the wax with a stylus, and then contacting the exposed glass surface with hydrofluoric acid for one to three minutes.

As Davis and Jones (1968) observed, the nature of flow patterns that can be generated by this "wax and stylus" technique is limited. They used a similar micromodel to study the displacement mechanism of micellar solution slugs. Instead of a wax coating, they used a photosensitive resist on the glass surface. In this manner any black and white pattern can be transferred to the surface. An additional modification has been made since the publication of their work. Jones (1980) described this modification in a personal communication to the author: instead of fusing the etched glass plate onto a cover plate, both plates are mounted in a pneumatically pressured cell. This modification allows fluid to be injected into the model at pressures as high as 60 psig.

Mast (1972) carried out a microscopic study of foam flow in porous media using etched glass micromodels similar to those of Davis and Jones (1968). For some models, the etching procedure was carried out twice. During the second etching procedure only some of the existing pores were etched again. Thus a system of large and small pores was obtained. The porous system was essentialy two dimensional: the flow paths were

channels with rectangular cross-sections.

A study of the multiphase flow of oil and water dispersed in porous medium was carried out by Bonnet (1978) using an etched plastic micromodel. Essentially, the technique involved transferring a pattern of pores to a plastic plate coated with a photo sensitive resist. The main drawback of this method is that grain size diameters less than 250 microns could not be achieved.

One of the problems with the etching techniques of these micromodels is that no adequate control of the resulting pore dimensions were achieved. This and other problems have been avoided in this work by using a micromodel consisting of etched silicon wafer. The model will be described in detail in Section 4, after describing the experimental apparatus in the next section.

3. EXPERIMENTAL APPARATUS

The experimental apparatus was designed and built to achieve three main objectives: the formation and flow of foam in a porous medium; the visual observation and study of the flowing foam; and the measurement of the pressure drop across the porous medium. Thus, the apparatus consists of a fluid flow system, an observation system, and a pressure measurement system. These will be described separately. Figure 3.1 is a schematic diagram of the apparatus.

3.1 FLUID FLOW SYSTEM

The fluid flow system includes a syringe pump, a micromodel and a liquid collector.

A low rate syringe pump advances a syringe piston at a constant rate. Fluid (water, surfactant solution, or air) to be injected into the micromodel is contained in the syringe. Injected fluids flow through a filter with a 2-micron element before contacting the micromodel. The actual input rate of the injected air must be calculated, taking into consideration the compressibility of the air, the varying injection pressures and the constant rate at which the syringe piston advances. The outlet pressure is at atmospheric pressure.

A syringe pump, Sage Series 237-2, was used for this experiment. Synchronous motors drive a set of drive and idler gears. The drive gear advances a carriage that moves a syringe piston at a constant rate. For a compressible fluid, the fluid discharge rate is different from the rate at which the piston advances.

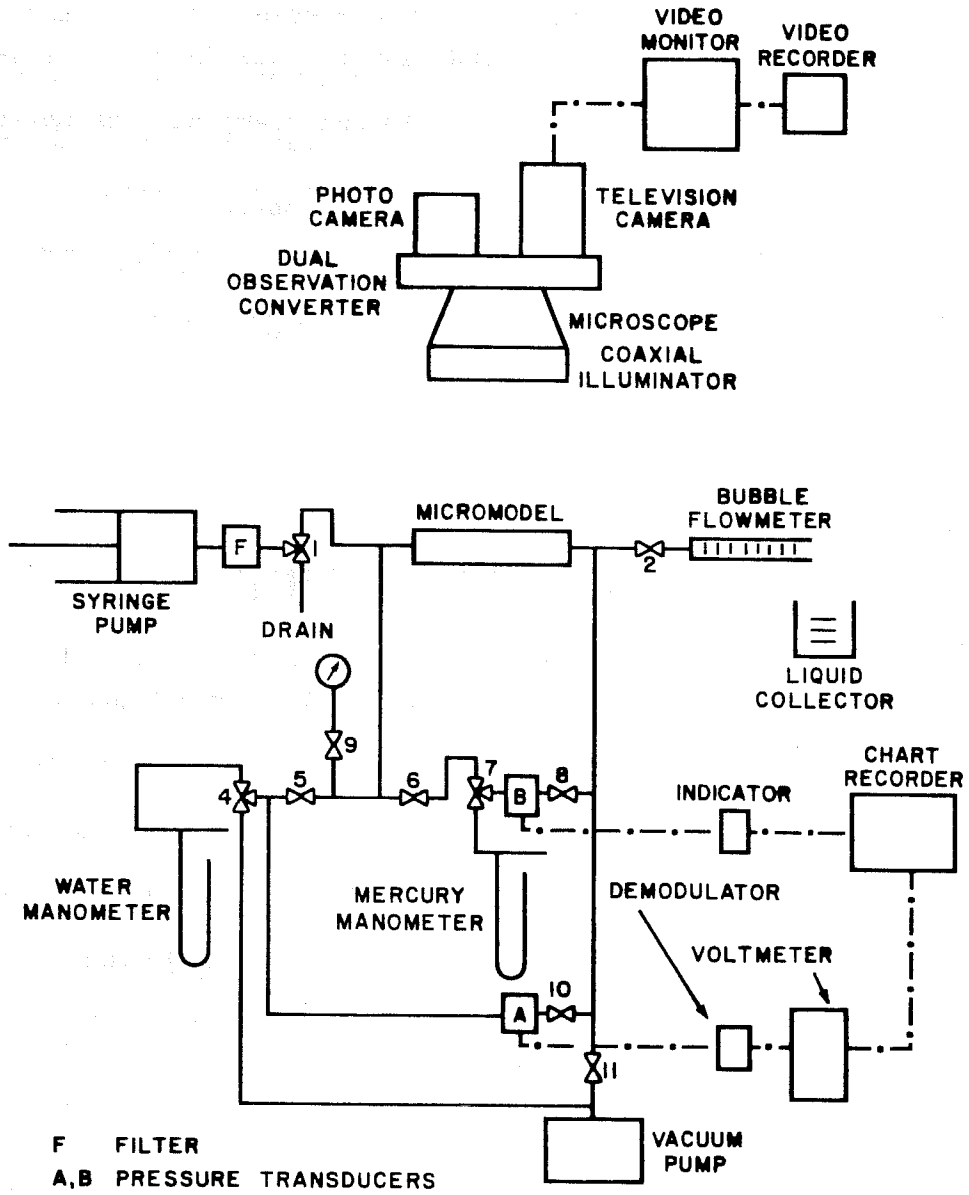

Fig. 3.1 SCHEMATIC DIAGRAM OF APPARATUS

Different nominal rates are available through one of the following processes: a change of syringe size, an interchange of the drive and idler gears, use of a ten-position transmission; or any combination of the three. The transmission varies the flow rate over a wide range for each syringe size. Throughout the experiment, the pump was calibrated for any chosen syringe size. A list of nominal rates given by the manufacturers for different syringe sizes is given in Table 3.1.

Fluid injected into the micromodel is visually observed during flow through the micromodel. The observation equipment is described next.

3.2 OBSERVATION SYSTEM

The purpose of the observation system is to view and document events in the micromodel. The upper half of Figure 3.1 shows the spatial arrangement of the major components: an illuminator, a cycloptic microscope, a dual observation system, a photographic assembly, a video monitor, and a video recorder.

The microscope has a binocular telescopic system which yields a stereoscopic image of the field of view. The working distance ranges from 3.8 to 11.2 cm depending on the eye piece and objective magnifications. The micromodel is an etched silicon wafer and is mounted on a glass stage at the base of the microscope. An internal coaxial illuminator attached to the microscope objective was used for lighting.

Light is transmitted through the eyepiece to two collecting lenses via a magnifier. Each collecting lens transmits light to a section of the dual-observation splitter. The latter feeds light to a phototube and a binocular head. Thus, there are two collecting lenses, two

Table 3.1

NOMINAL FLOW RATES FOR SYRINGE PUMP 237-2

	Flow Rate, cc/s x 10^4 *			
SYRINGE SIZE	10cc	5cc	2cc	1cc
DRIVE GEAR (100% SETTING)				
Small	61.0	39.0	23.1	6.39** 6.32
Large	156	100	60	16

NOTE: * The flow rates are expressed in cc x 10^{-4}/s. This notation is equivalent to cc/s x 10^4. Both appear in this report.

** Measured value.

phototubes and two binocular heads. The binocular heads are for direct viewing while the phototubes are adapted for cameras.

Two cameras, a 35 mm camera, and a video TV-camera are mounted on the photographic tube adapters. A black and white 9-in. diagonal video monitor is connected to the input of a VHS video recorder. The linear magnification of this system depends on the objective-eyepiece combination and the setting of a magnification-changer attachment. Typically, the system view-field ranges from 0.7 x 0.7mm to 3.2 x 3.2mm.

3.3 PRESSURE MEASUREMENT SYSTEM

Compared to other fluids, flowing foam produces a characteristic high pressure drop in a porous medium. In this experiment, pressure drop across the micromodel was accurately monitored while the outlet pressure was kept at atmospheric pressure.

Two KP-15 differential pressure transducers are connected in parallel to measure the pressure drop across the micromodel. The lower half of Figure 3.1 is a schematic drawing of the pressure measuring equipment. A demodulator converts the pressure drop into an electrical signal which is read from a voltmeter output (0 to 10 volts). The voltmeter's output is connected to a chart recorder for continuous recording of the pressure drop. Diaphragms of different ratings were used in the two transducers. The parallel connection of these transducers enables either of the diaphragms to be used, depending on the range of pressure drop seen. This minimizes the measurement errors. Calibration of the transducers is done in situ with either a water or a mercury manometer.

In the above description of the apparatus, a major component, the micromodel, has not been included. The next section presents a detailed description of the models used.

4. THE MICROMODELS

Two types of micromodels, homogeneous and randomly distributed pore structures, were used for the experiment. A detailed description of the fabrication and assembly of the models is given in Appendix A. The following topics will be covered here: a general description, a characterization of the pore structure, and an analysis of the fluid flow through the models.

4.1 GENERAL DESCRIPTION

The following description applies to all the micromodels. Each model consists of an etched silicon wafer in which a monolayer of porous matrix has been simulated. A layer of silicon dioxide was thermally grown on the silicon wafer in order to achieve a wettability similar to natural porous media. Figure 4.1, drawn to scale, is the fluid flow area of the micromodel. The large central area, (d)(a), of the figure is a network of etched flow channels. The flow channels interconnect a system of unetched solid matrix. Thus the channels replicate the pore spaces and the unetched matrix constitutes the sand grains of a porous medium (as in petroleum reservoirs). Input and output channels, (ℓ)(b), are provided on opposite ends of the porous matrix. Two rectangular end portions are etched to provide for fluid injection and production.

Fluid distributing channels (about one pore space in width) were etched adjacent to the porous matrix. They allow fluid displacement to occur uniformly across the model. The fluid distributing channels are shown in Fig. 4.2a for the homogeneous models and Fig. 4.4a for the heterogeneous model.

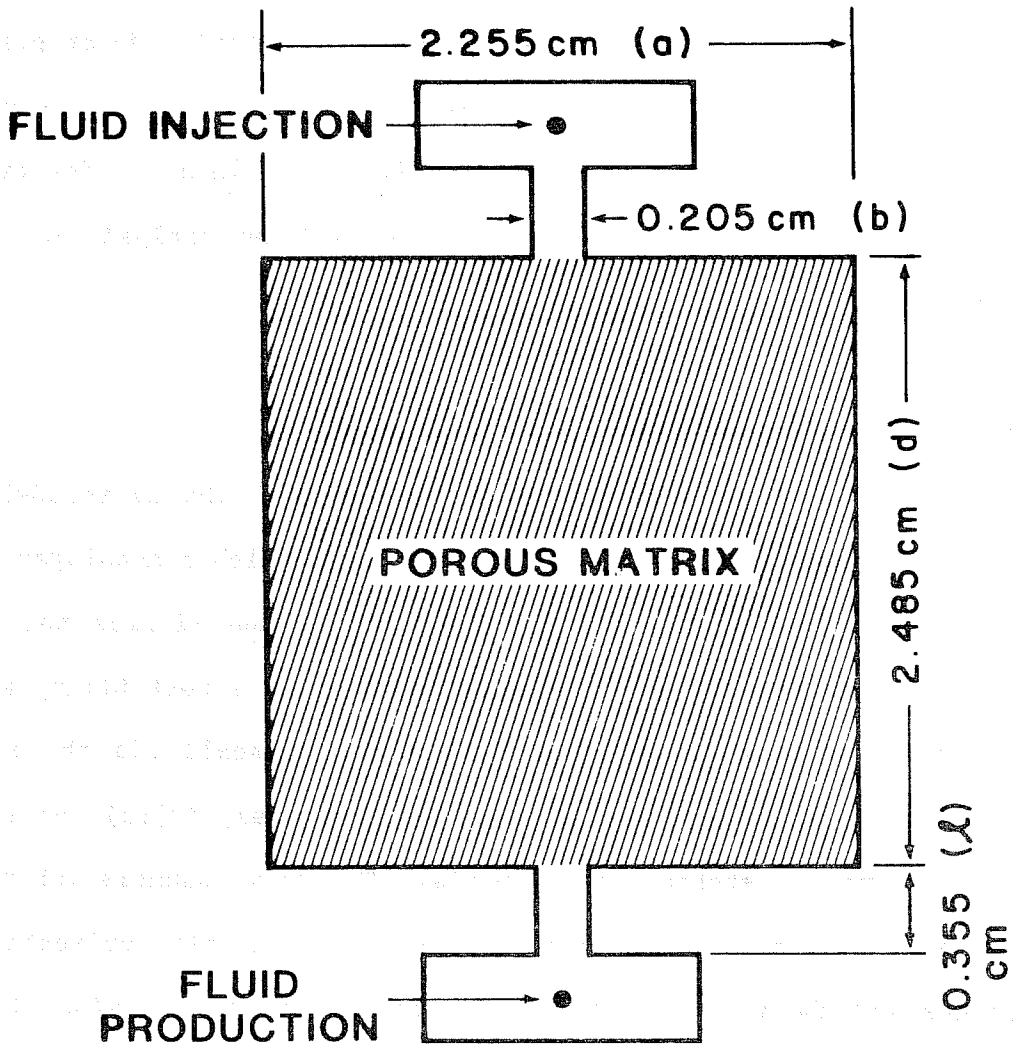

Fig. 4.1 FLUID FLOW AREA OF THE MICROMODEL

The fluid flow area described above is permanently sealed with a flat glass cover-plate anodically bonded to the silicon wafer. Fluid injection and production are through tubes connected to holes drilled through the cover plate at the injection and production points.

4.2 MICROMODEL PORE STRUCTURE

The two sets of micromodels used for these experiments differ in the shape, size and distribution of the simulated matrix grains and flow channels (pore system). The homogeneous micromodels have uniform matrix grains that are evenly spaced and distributed. In the heterogeneous model, the matrix grains and pores are non-uniform in size, shape and distribution. The two models will be described separately.

4.2.1 Homogeneous Model (OW.200)

Figures 4.2a and 4.2b are electron scanning micrographs of the micromodel's pore structure. The "sand grains" are truncated right circular cones whose centers are in a hexagonal, close-packed array. These matrix grains are uniform in size and are separated by an evenly distributed network of interconnecting channels. The channels are etched to a uniform depth of 30 microns. Between any three matrix grains is a large pore area labelled "p". This pore area is generally referred to as the pore body. The spacing, n, between matrix grains is called the "pore neck". Because of the shape (frustrum) of the sand grains, the pore neck tapers to a minimum value at the base of the flow channels. Thus, the ratio of the pore body diameter to the pore neck, p/n, is a function of the flow channel depth. This is summarized in Fig. 4.3 for the three homogeneous (pore system) micromodels used.

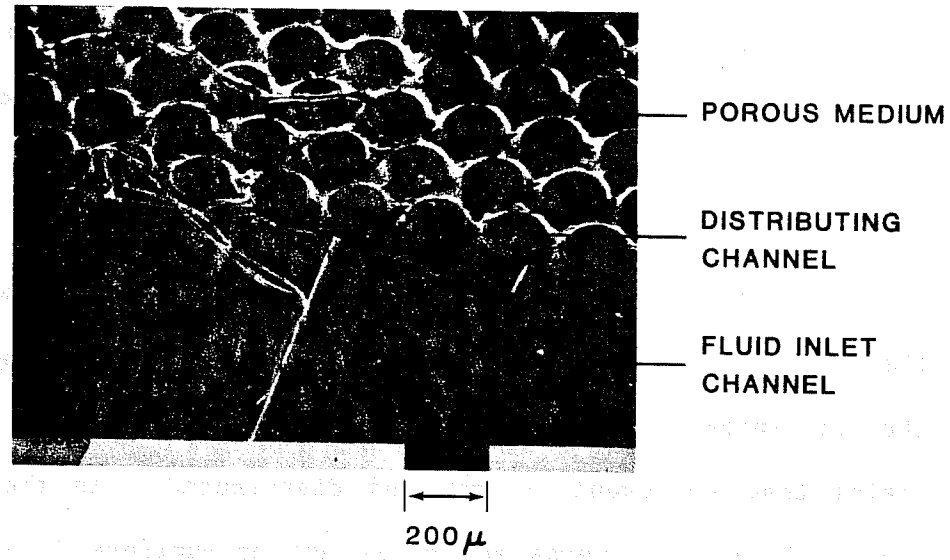

Fig. 4.2a HOMOGENEOUS PORE STRUCTURE: A GENERAL VIEW

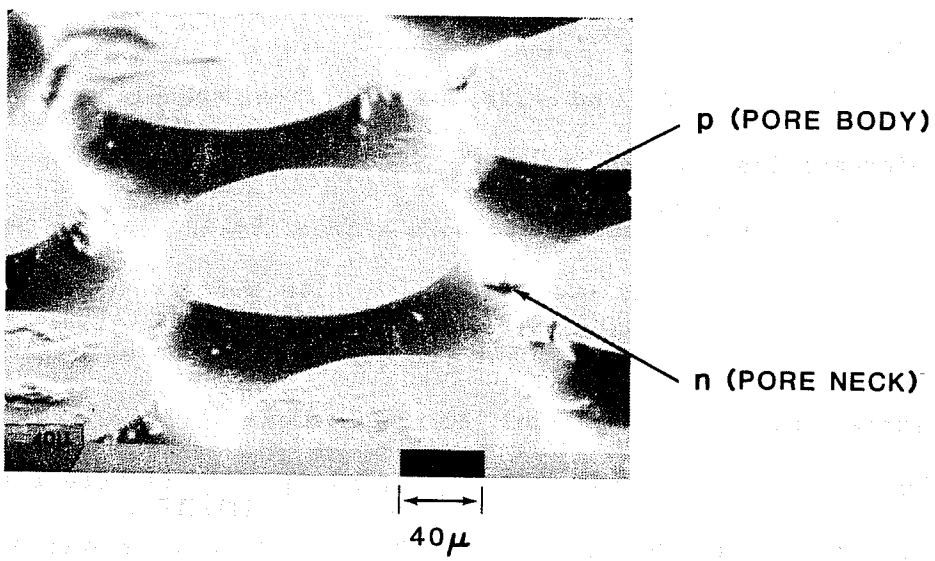

Fig. 4.2b HOMOGENEOUS PORE NETWORK

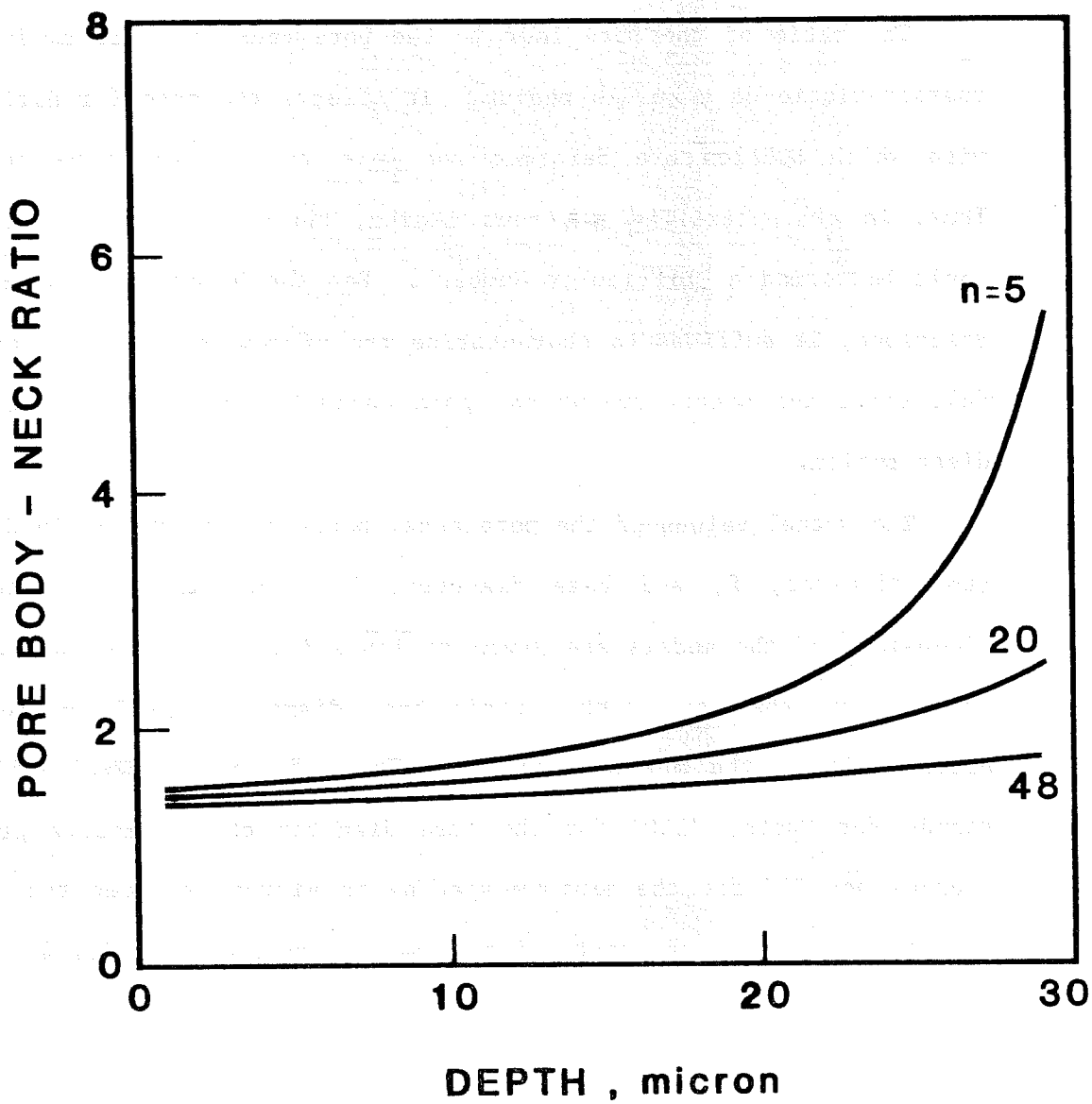

Fig. 4.3 CHARACTERIZATION OF PORE STRUCTURE: HOMOGENEOUS MODEL

These models are characterized by the minimum values of their pore necks. The location of the minimum pore spacing is shown symbolized by "n" in Fig. 4.2b.

The ratio of the pore body to the pore neck, p/n, is an important characteristic of a porous medium. It affects the ease (or difficulty) with which bubbles are deformed and move through the pore channels. Thus, in characterizing a porous medium, the pore body to neck ratio could be termed a "Difficulty Number". For the homogeneous pore system described, it suffices to characterize the micromodels by the pore neck (n), since the matrix grains and pore channels are uniform in size and distribution.

The actual values of the pore neck, porosity, matrix grain diameter (top diameter, f, and base diameter, D), and other characterizing dimensions of the models are given in Table 4.1. The three homogeneous models have the same matrix grain base diameter of 200 microns and differ only in the minimum spacing. Thus, for model "OW.200.5", "OW" stands for Owete, "200" for the base diameter of the matrix grain in microns and "5" for the minimum spacing in microns between the grains. The porosity, ϕ, is calculated from simple geometry using Eq. 4.1:

$$\phi = 1 - \frac{\pi\,(f^2 + fD + D^2)}{6\sqrt{3}\,(D + n)^2} \qquad (4.1)$$

Table 4.1

MICROMODEL PROPERTIES

MODEL	GRAIN SIZE (D) (μm) Bottom	GRAIN SIZE (D) (μm) Top	BOTTOM SPACING (n) (μm)	DEPTH (h) (μm)	PORE BODY TO NECK RATIO (p/n) (Ratio)	POROSITY (ϕ) (%)	ABSOLUTE PERMEABILITY (k) (darcy)
OW200.5	200	165	5	30	7.3*	28	0.7
OW200.20	200	166	20	30	2.7*	32	3.0
OW200.48	200	168	48	30	1.8*	47	4.3
OW.HET	1-150		20**	5	2.5-5.0	60	1.6

* Maximum Values (Ref. Fig. 4.3).

** Average Value.

4.2.2 Heterogeneous Model (OW.HET)

Figures 4.4a and 4.4b show the pore structure of the heterogeneous micromodel. The "sand grains" are non-uniform in size, shape and distribution. They have slanting walls with a slope of 55 degrees. The equivalent grain diameter ranges from 1 to 150 microns or more. The matrix grains are separated by an interconnected network of flow channels.

The flow channels are randomly distributed in size and shape. They are etched to a depth of 5 microns. Between two or more matrix grains, there exists a pore body area (area of maximum pore opening). The pore body varies in maximum dimensions from 50 to 100 microns throughout the model. Between any two pore bodies, the flow channel attains a minimum opening at some point. The areas of minimum pore space constitute the pore necks. The pore necks for this model have an average value (spacing) of 20 microns. Thus, the ratio of the pore body spacing to the pore neck spacing varies from 2.5 to 5.0.

Figure 4.4b shows the heterogeneous pore system, the pore body and neck areas and some dead end pores. The dead end pores resulted from the non-uniformity in the shape and distribution of the matrix grains. Although few compared to the frequency of occurrence in natural pore systems, the dead end pores in this heterogeneous model represents an improvement over the homogeneous models. In petroleum reservoirs, fluid retention occurs at the dead end pores, and causes residual saturations. Another improvement is the close spacing of some of the grains. However, there are no grain contacts. Grain contacts in real systems cause liquid hold up during air-liquid displacement, and hence reduce the mobility of the flowing fluids.

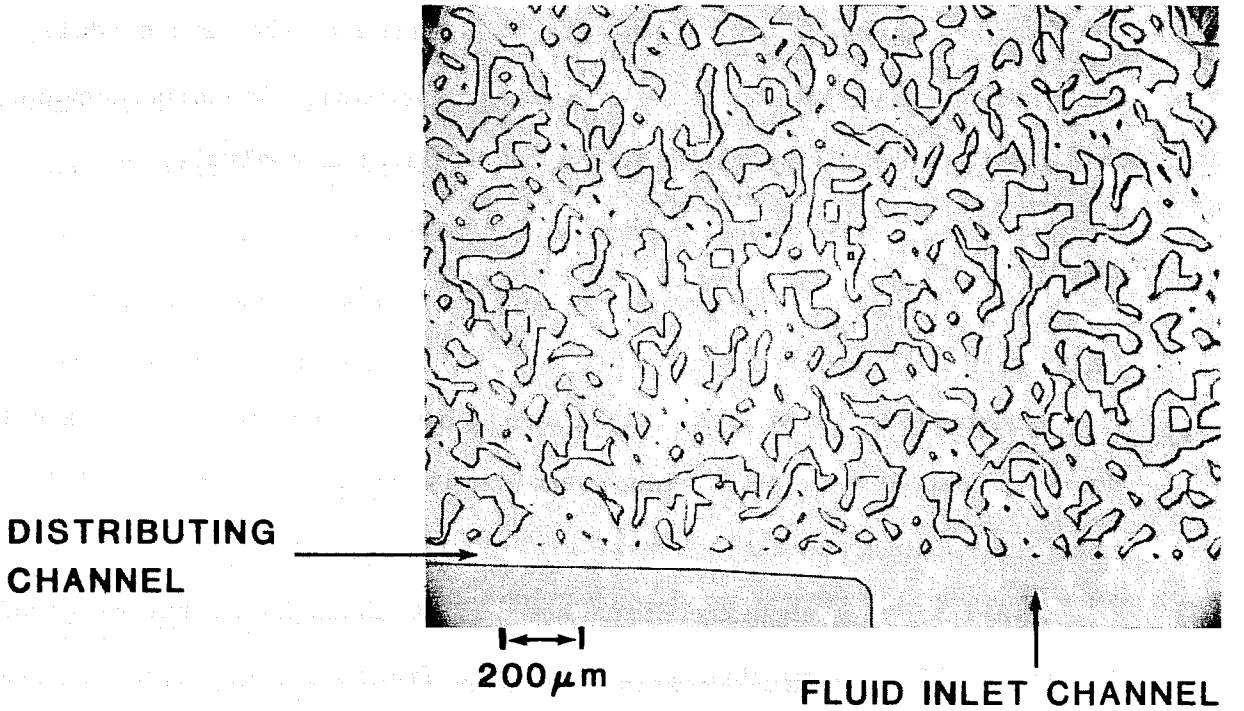

Fig. 4.4a HETEROGENEOUS PORE STRUCTURE: A GENERAL VIEW

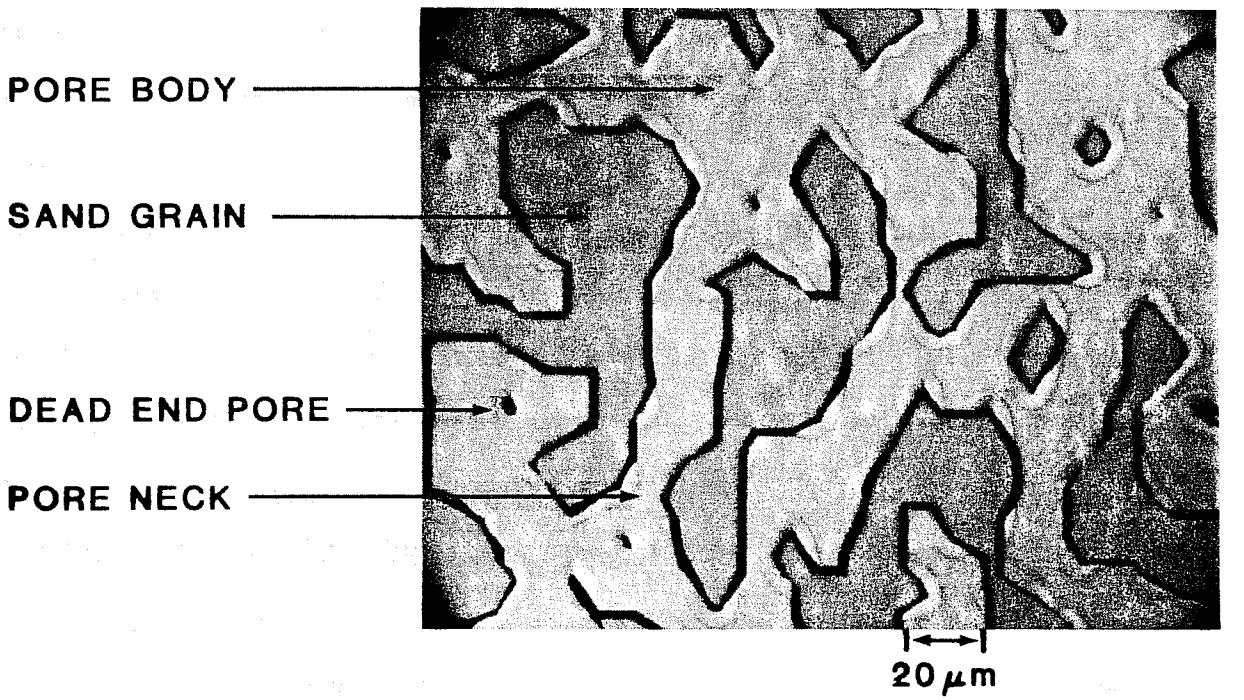

Fig. 4.4b HETEROGENEOUS PORE NETWORK

Before studying the flow of foam through the micromodels, an analysis of resulting fluid flow patterns was made. The displacement of fluid with a unit mobility ratio was used for the analysis, and this is the subject covered in the following section.

4.3 FLUID FLOW ANALYSIS.

A detailed analysis of the flow patterns in the micromodel and the development of the fluid flow equation is given in Appendix B.1. A brief description of the analysis will be given here.

Fluid flow through the input and output channels in the micromodel is essentially a flow through a slot or a fracture: the channels have a width-depth ratio of approximately 70 for the homogeneous models, and 420 for the heterogeneous model. The pore spaces in the large central portion, (d)(a), in Figure 4.1, are interconnected and continuous from the input channel to the output channel. This constitutes a "direct line drive" pattern. In approximating the flow system as a "direct line drive", the effect of the distributing channels (Figs. 4.2a and 4.4a) was neglected. A large distributing channel will cause a linear flow in the central portion of the model.

The model can be described as three layers in series. Fluid injected into the model flows through a fracture and then enters a direct line drive pattern. It flows out of this pattern into an outlet fracture. By adding up the pressure drop in the three sections, a final flow equation for a fluid displacement of unit mobility ratio is given as follows:

$$k_d = \frac{1076\ (\log \frac{a}{b} + 0.682\ \frac{d}{a} - 0.196)}{h\ (\frac{\Delta p}{\mu q} - \frac{\ell}{278000\ bh^3})} \qquad (4.2)$$

where k_d is the absolute permeability of the model, millidarcies

Δp = the total pressure drop across the model, psi

μ = the viscosity of the flowing fluid, c_p

q = the flow rate, cc/s

h = the etched depth of the model, cm

a, b, d, and ℓ, the external dimensions of the flow area in cms, are as shown in Fig. 4.1.

5. EXPERIMENTAL PROCEDURE AND CALCULATIONS

Visual observations of air-water and air-surfactant displacements were made to study the general flow behavior of in situ generated "foam." The mobility of air in the presence of water and foam was measured. This section describes the experiments and the surfactant used for this study. The method used in calculating the mobility of air is also described.

5.1 EXPERIMENTAL PROCEDURE

The absolute permeability of each micromodel was determined with water flow at 100% saturation using Equation 4.2. Control experiments were then made by displacing the water with air. For the foam studies, foam was generated in situ by injecting air into the model which had been previously saturated with an aqueous solution of surfactant. The same procedure was used for the water runs as for the surfactant runs.

First, the micromodel and the flow lines leading to the pressure differential transducers were evacuated. Water or surfactant solution was then injected into the model and the flow lines with the syringe pump. Next, the transducers were calibrated using mercury and/or water manometers.

For a selected pump air injection rate (constant piston displacement rate or nominal rate), air was injected into the micromodel to displace the liquid. The pressure drop across the model was continuously monitored during displacement. The displacement was recorded by means of a video monitor.

As stated in Section 4, three homogeneous micromodels and one heterogeneous model were used for this study. Each homogeneous model has a different characteristic pore dimension. Different nominal air injection rates were used. In investigating the influence of pore dimension and nominal air injection rate, a 1% (weight active) aqueous surfactant solution was used. Using model OW.200.5 (one of the homogeneous models), the effect of surfactant concentration on the flow behavior of foam was studied. Both rate and concentration studies were done using the heterogeneous model (OW.HET).

All the experiments were performed at room temperature. The surfactant (foaming agent) used is described next.

5.2 FOAMING AGENT

The foaming agent used for all the experiments was Suntech IV. The surfactant is a petroleum sulfonate made directly by sulfonation of a refinery stream. The preparation and properties have been described by Malmberg and Burtch (1979).

The surfactant was supplied in batches containing different amounts of surface active material. Surfactant concentration was measured using the "Hyamine" titration method described by Reid, et al. (1967). The surface tension of the aqueous solution was then determined as a function of concentration using a ring surface tensiometer. The results are displayed in Fig. 5.1. The surface tension decreases with increasing concentration. The point where a break occurs in the surface tension vs concentration profile corresponds to the critical micellar concentration (CMC) of the surfactant. The batches referred to as "OLD" and "NEW", after Sharma, et al. (1982), and the "PILOT TEST" batch were used in this work.

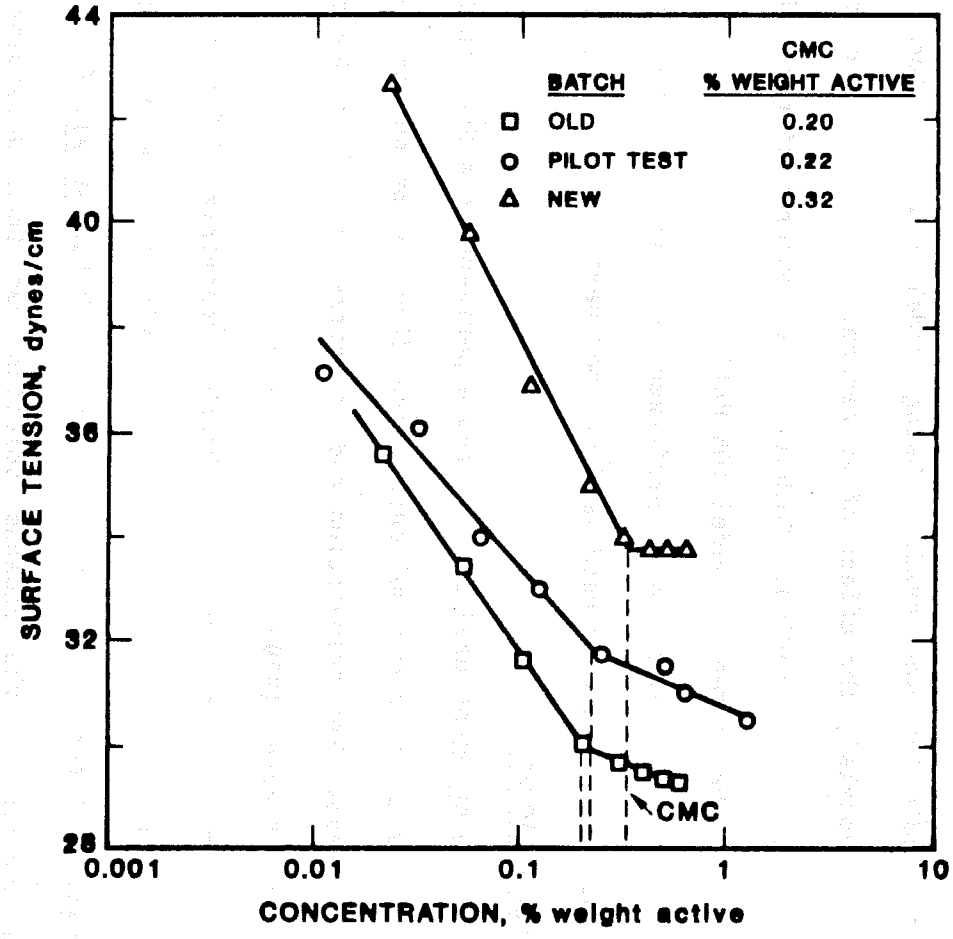

Fig. 5.1 CONCENTRATION-SURFACE TENSION PROFILES FOR SUNTECH IV

Regardless of the surfactant concentration used, the performance of the displacement was measured by the mobility of air at different pore volumes of injection. The following section outlines the procedure used in calculating air volume and flowrate during the displacement.

5.3 CALCULATION PROCEDURE

When water or surfactant solution is displaced by air, the pressure drop (Δp) across the micromodel is monitored as a function of time (t). From the pressure drop/time data, the following are computed:

1. the cumulative volume of air injected,
2. the air flowrate in the porous medium, and
3. the effective mobility of the injected air.

By material balance on the initial volume of air (V_s) in the syringe, the cumulative volume of air (Q_a, at atmospheric pressure) injected into the model is obtained from the following equation:

$$Q_a = \frac{p_s V_s}{p_a} - \frac{(V_s - Rt)(p_a + \Delta p)}{p_a} \qquad (5.1)$$

where Q_a is the cumulative volume of air injected into the model (at atmospheric pressure), cc

p_s = initial syringe pressure, psia

p_a = atmospheric pressure, psia

V_s = initial volume of air in the syringe, cc

R = constant, nominal syringe pump rate, cc/s

t = time, s

Δp = total pressure drop across the model, psi

Equation 5.1 is differentiated with respect to time (t) to obtain the actual air flow rate at the inlet end of the model. This is given in Eq. 5.2:

$$q_a = R\left(1 + \frac{\Delta p}{p_a}\right) + \frac{Rt - V_s}{p_a}\left(\frac{d(\Delta p)}{dt}\right) \qquad (5.2)$$

The derivation of Eqs. 5.1 and 5.2 is given in Appendix B.2.

For a given time interval, some volume of air, ΔQ_a is injected into the micromodel. Over the incremental volume of air, ΔQ_a, let p_1^* and p_1^{**} be the lower and upper limit of the inlet pressures. To obtain the average inlet pressure $\bar{p}_1$ over the time interval, the inlet pressure is graphed versus the cumulative volume of air Q_a injected. Such a graph is shown in Fig. 5.2. Vertical lines which intersect the pressure curve at p_1^* and p_1^{**} are drawn. The average inlet pressure $\bar{p}_1$ corresponds to the intersection point which determines equal areas A_1 and A_2 as shown in Fig. 5.2.

Since the average inlet pressure $\bar{p}_1$ over the time interval of interest and the outlet pressure p_a are known, the average pore pressure $\bar{p}$ is obtained on that same time interval from Eq. 5.3:

$$\bar{p} = \frac{\bar{p}_1^2 + p_a^2}{2p_a} \qquad (5.3)$$

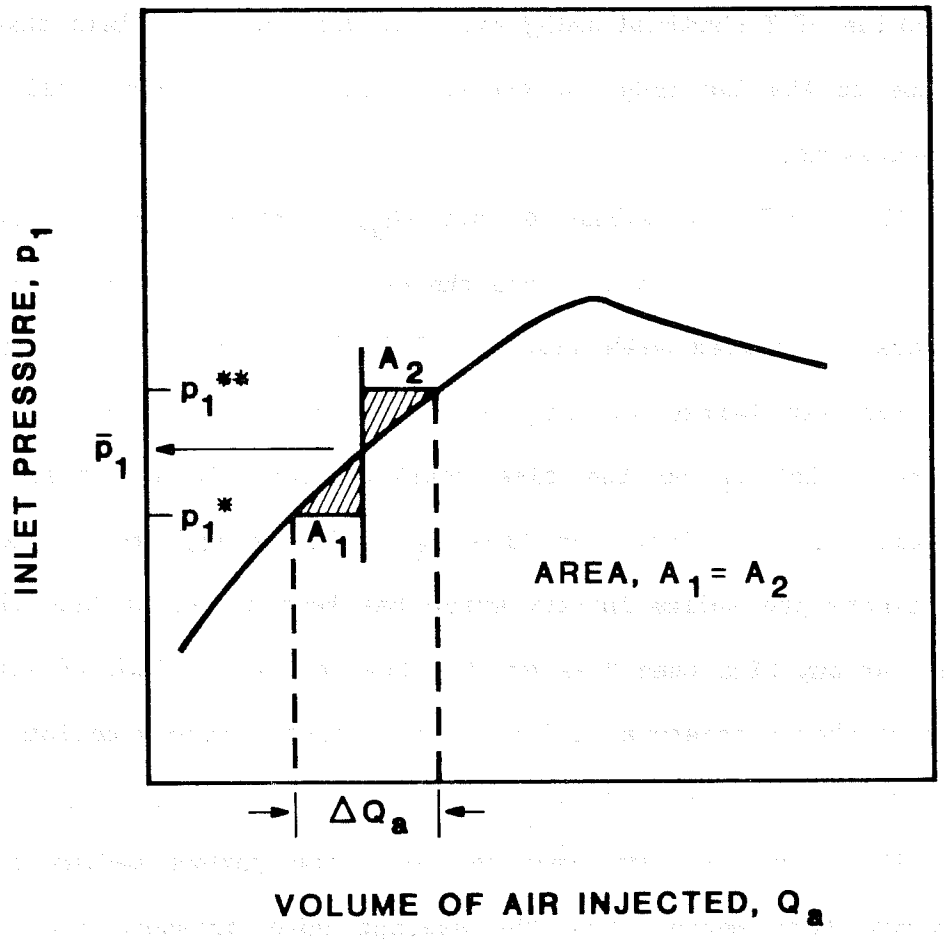

Fig. 5.2 DETERMINATION OF AVERAGE INLET PRESSURES

When an arithmetic average was taken between $\bar{p}_1$ and p_a and compared to the value of $\bar{p}$ obtained using Eq. 5.3, the error was less than 1%. This is due to the low range of pressure drops (less than 5 psi) during the displacement.

The cumulative volume of air (Q_a) obtained from Eq. 5.1 includes the volume of air injected into the entry headers. Initially, the entry headers are filled with liquid. This liquid must be displaced by the injected air before air-liquid displacement can occur in the porous medium. Let t_E be the time required for air to enter the porous medium. Q_a calculated at time t_E will be referred to as Q_{aE}, and represents the volume of air which has been injected into the headers. Thus, at any time when t is greater than t_E, the volume of air (measured at atmospheric pressure, p_a) injected into the porous medium is Q_a minus Q_{aE}.

The volume of air injected into the porous medium and the air flowrate both measured at the average pore pressure are obtained as follows:

$$\bar{Q} = \int_{Q_{aE}}^{Q_a} \frac{p_a}{\bar{p}} \, \Delta Q_a \qquad (5.4)$$

$$\bar{q} = \frac{p_a}{\bar{p}} q_a \qquad (5.5)$$

Finally, the pore volumes of air injected and the effective air mobility are obtained using the following relationships:

$$\text{Pore Volume of air injected} = \bar{Q} / V_p \qquad (5.6)$$

$$\text{Effective air mobility} = \bar{q}/\Delta p \qquad (5.7)$$

V_p is the pore volume of the micromodel. Appendix B.3 provides an error analysis on the use of the preceding equations. In the next section the results of the experiments are presented.

6. RESULTS

The porosity, absolute permeability and other properties of the micromodels are shown in Table 4.1. Two types of porous media, homogeneous and heterogeneous, were used for this study. The data obtained from the air displacement experiments consists of two parts:

1. Visual observation of fluid propagation.
2. Effective air mobility obtained from the pressure drop-time data.

The following sections will describe fluid propagation and effective air mobility in both the homogeneous and heterogeneous pore systems. In all experiments described, surfactant concentration refers to the per cent by weight of surface active material present in an aqueous solution of the surfactant.

6.1 FLUID PROPAGATION

Fluid flow in the micromodels was observed for air-water displacements and for air-surfactant solution displacements at different concentrations. The distribution and propagation of fluids differed in the two types of micromodels. In the heterogeneous model, the flow behavior differed with changes in surfactant concentration. The observed fluid flow characteristics will be presented separately for each type of model.

6.1.1 Homogeneous Model

Figures 6.1a-c show the fluid distribution in the porous medium for air displacing 1% surfactant solution in model OW.200.20 at a nominal

air injection rate of $2.56(10^{-4})$ cc/s. A network of liquid (dark films) surrounds the matrix grains (the bright circular portions). The liquid is continuous throughout the porous medium via the grain-liquid and air-liquid interfaces (liquid membranes).

The air-liquid interfaces are oriented in two ways with respect to the general flow direction: slanted, forming a diagonal surface between diagonally offset matrix grains, and horizontal, forming a surface between two adjacent matrix grains perpendicular to the flow direction. These membranes will be referred to as "diagonal" and "horizontal" interfaces respectively.

The horizontal interfaces are unstable and are displaced in the flow direction as the pressure in the system builds up. Thus, the horizontal interfaces of Fig. 6.1a have disappeared a short time later (Fig. 6.1b). The diagonal interfaces, which form early in the displacement, tend to retain their positions and orientation. The thicknesses of the diagonal liquid membranes, however, decreases with time. This indicates that the liquid is drained continuously through this network.

The air is propagated in a different manner. The diagonal interfaces define and limit the air flow paths. An air channel in an advanced stage of the flow can be seen in Fig. 6.1c. The air occupies and flows through the pore spaces, leaving the liquid confined in films around the matrix grains. The air channels are only occasionally broken in continuity by horizontal interfaces. In this way, leading and trailing fluid interfaces develop which enclose tubular bubbles.

For the homogeneous models used in the experiment, horizontal interfaces which formed in early stages of air displacement were not

FLUID PROPAGATION: MODEL 200.20

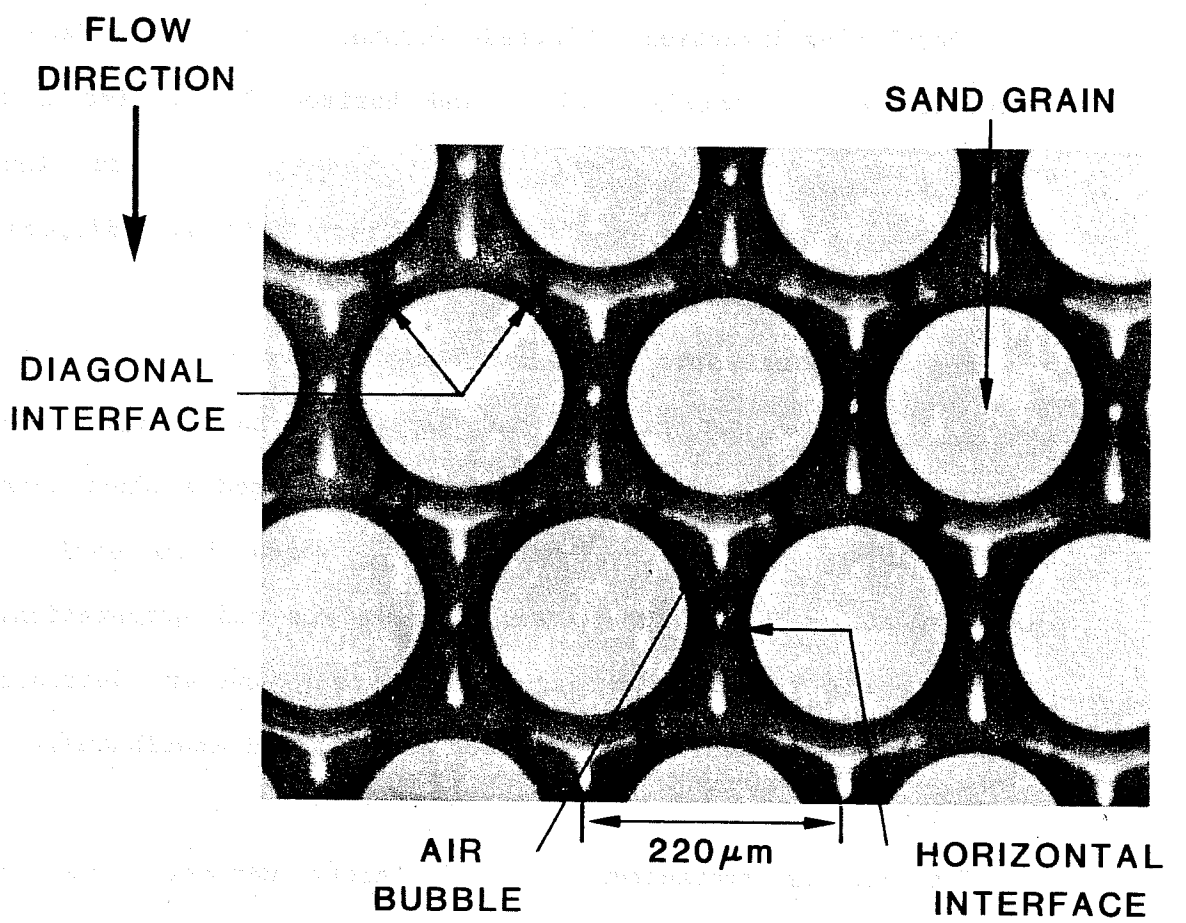

Fig. 6.1a FORMATION OF DIAGONAL AND HORIZONTAL INTERFACES

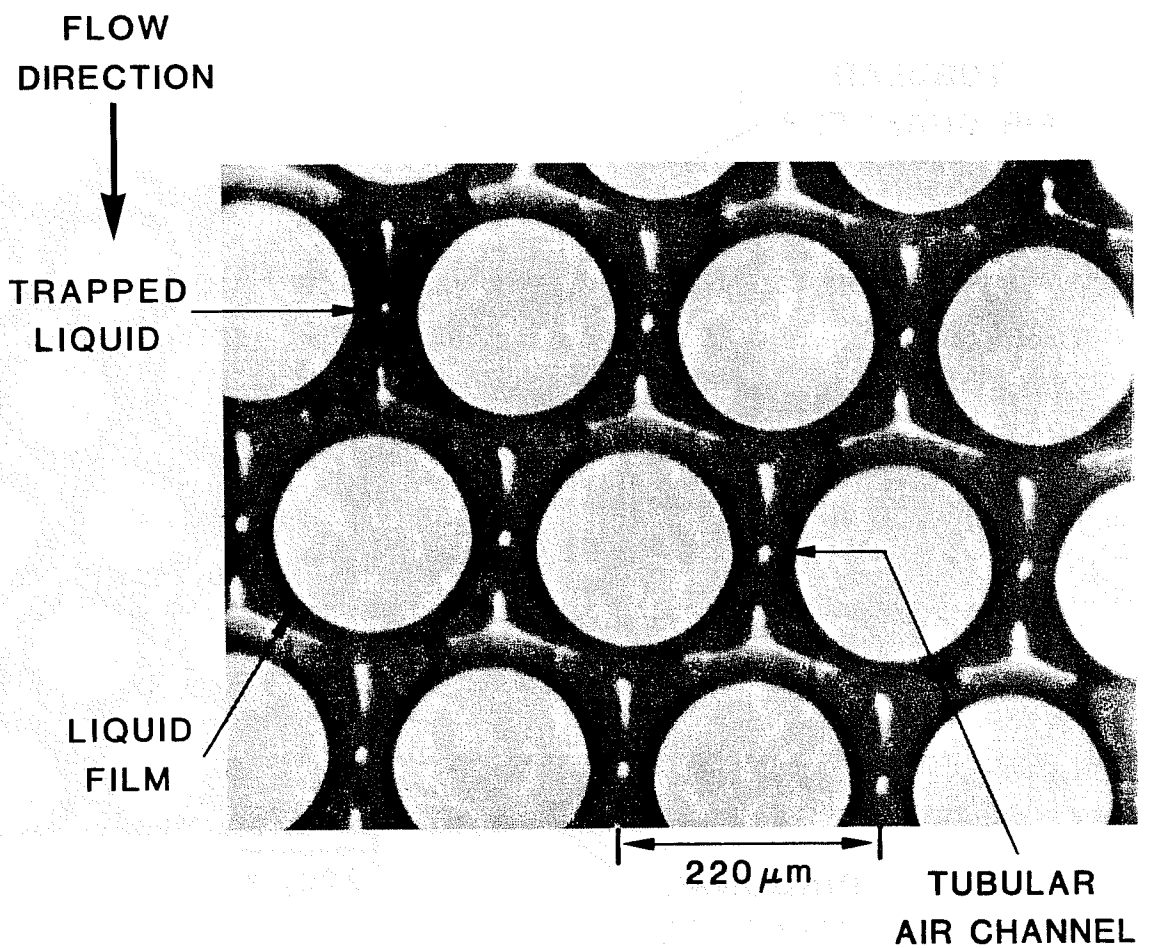

Fig. 6.1b LIQUID NETWORK AND TRAPPED LIQUID

FLUID PROPAGATION: MODEL 200.20

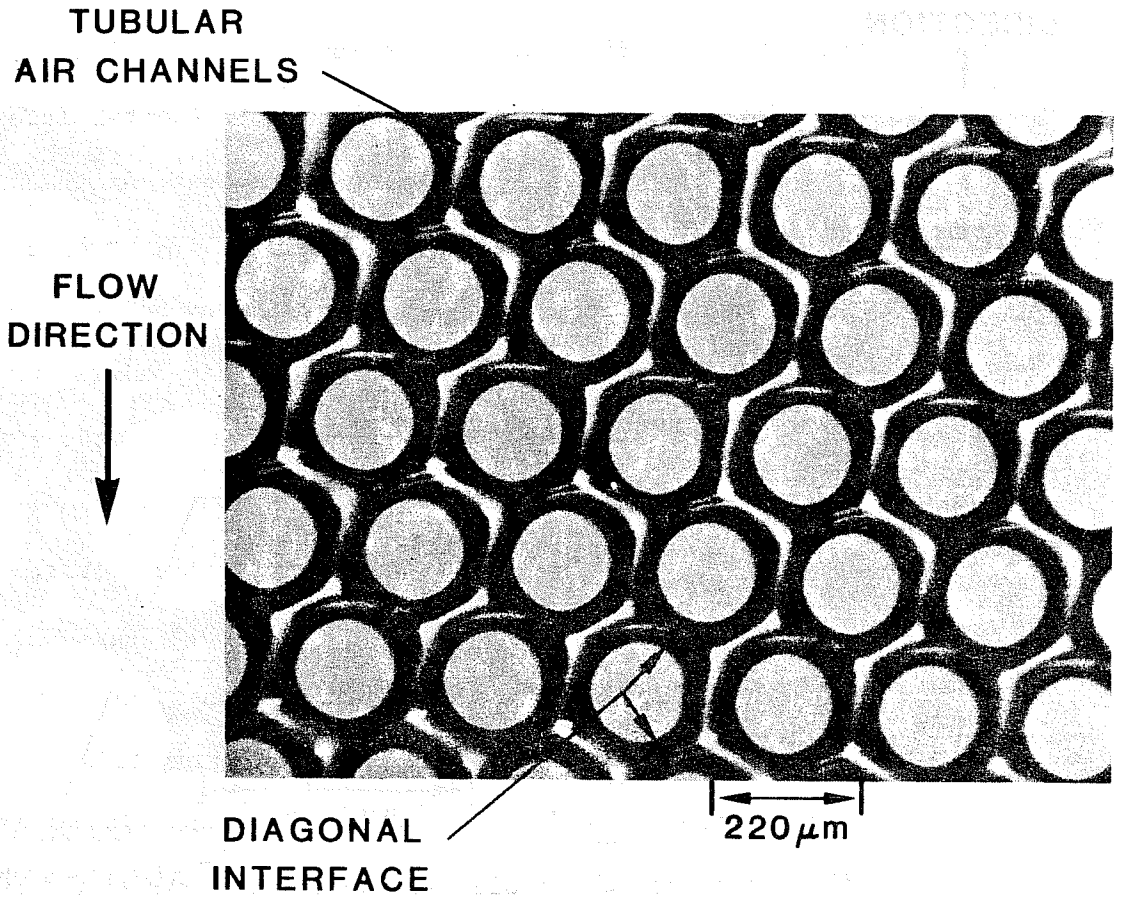

Fig. 6.1c TUBULAR AIR CHANNELS AND DIAGONAL INTERFACES

significant. The air-liquid front in a given pore channel occasionally flows backwards through some pores in a direction opposite to the general flow direction. Such flow leads to the trapping of liquid and air in some pores. Figure 6.1b shows such a trapped liquid patch.

The flow behavior shown in Figs. 6.1a-c is typical for the air injection rates and surfactant concentrations used in the homogeneous micromodel experiments. High air injection rates tend to produce instabilities at the displacement front, and more horizontal interfaces are formed compared to the number seen at low air rates. At the low air rates, the long continuous air channels, defined by the diagonal interfaces, are dominant. Pore dimension effects are similar to the effect caused by air injection rate: small pore dimensions have the same effect as low air injection rates. However, the variations due to flowrate and pore spacing (in the range studied) in the micromodels did not seem to change the basic mechanism of the displacement significantly.

Figures 6.2 show typical fluid distributions observed when different surfactant concentrations ranging from 0.001 to 1.0% were used in one of the homogeneous models, OW.200.5. A change in surfactant concentration did not affect the basic flow mechanism over this range of surfactant concentrations. In the heterogeneous model, however, surfactant concentration had an effect on the nature of the fluid generated and on the propagation of air and liquid. The following section describes the flow behavior in the heterogeneous model.

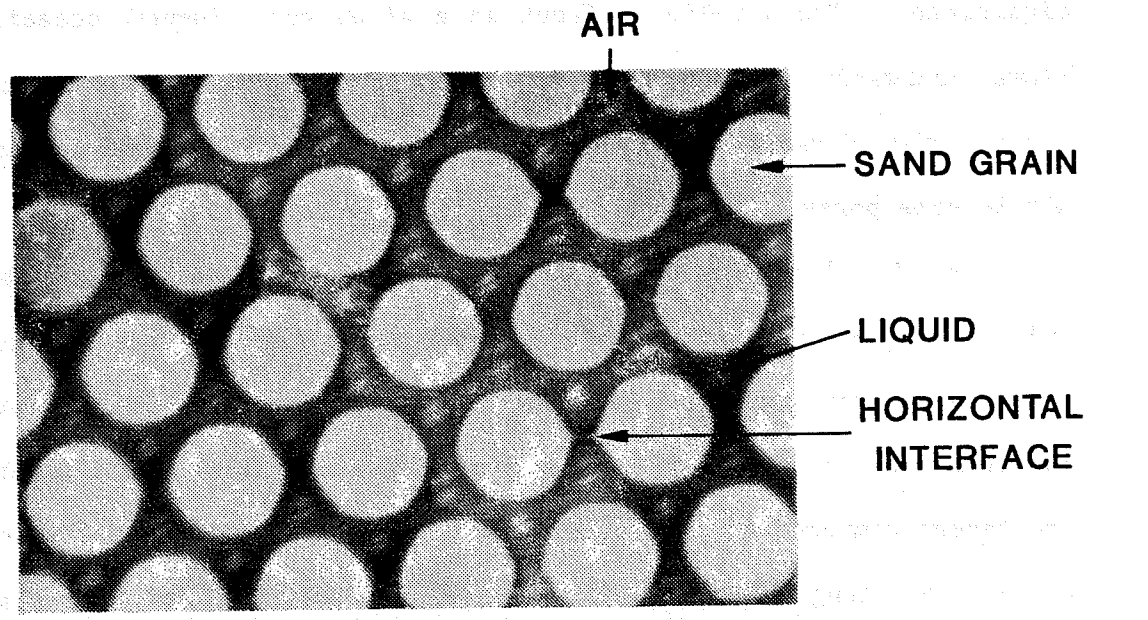

Fig. 6.2a Early Stage of Displacement

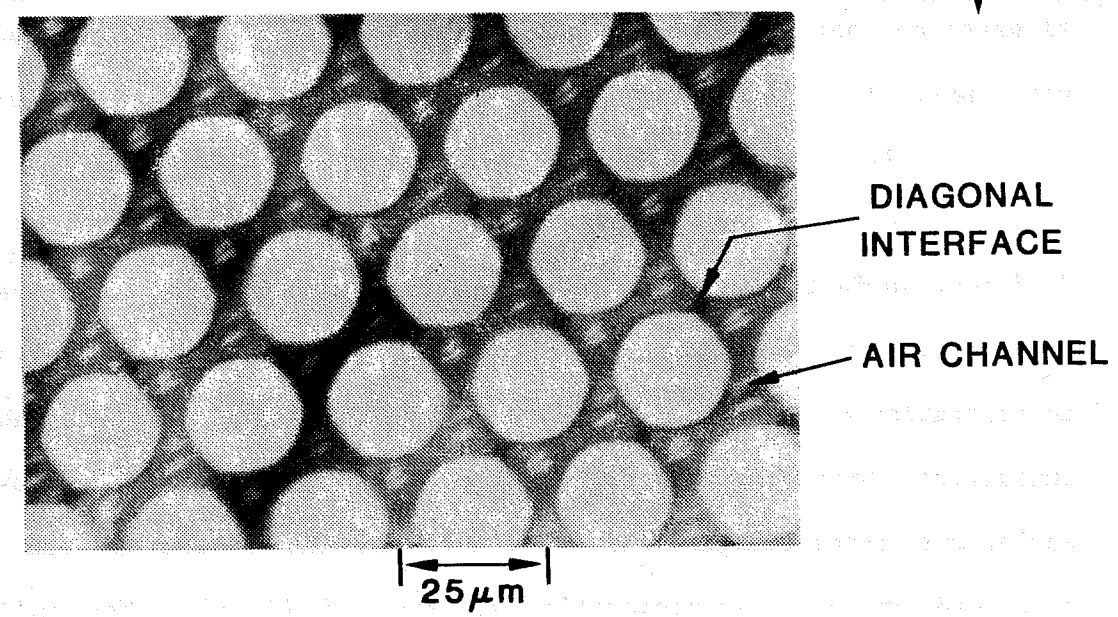

Fig. 6.2b Advanced Stage of Displacement

Fig. 6.2 TYPICAL FLUID PROPAGATION FOR VARIOUS SURFACTANT CONCENTRATIONS: HOMOGENEOUS MODEL (OW.200.5)

6.1.2 Heterogeneous Model

The fluid flow behavior described in this section is for air-liquid displacement in the heterogeneous model. A nominal air injection rate of 1.28 (10^{-4}) cc/s was used. First, air-water experiments were conducted.

Figures 6.3 show the distribution of air and water in the heterogeneous porous medium. Air displaced water from the pore spaces to form continuous air channels. As the air channel approached dead end pores, water was trapped. There was considerable tortuosity as the air flowed in different directions through several pores. Choke-off, a separation of a large bubble into a small droplet, was not observed and existing fluid interfaces were seen randomly between air channels. Fluid interfaces were also seen at the displacement front and at the entrances to dead end pores.

Air was injected into the heterogeneous micromodel that had been completely saturated with surfactant solutions of various concentrations. First, a surfactant solution of 0.001% concentration was used. A typical distribution of gas and liquid zones is shown in Fig. 6.4. Liquid was confined or trapped in small pores and dead end pores. Compared to water runs, air-surfactant (0.001%) displacement showed a higher displacement efficiency. In Fig. 6.4 the large pores have been occupied by air. Air-liquid interfaces and liquid membranes separating air channels appear mostly at pore neck areas. The mechanism represents a transition between the air-water flow behavior and the displacement mechanism for a 0.031% surfactant concentration described next.

When air was injected into the heterogeneous model saturated with

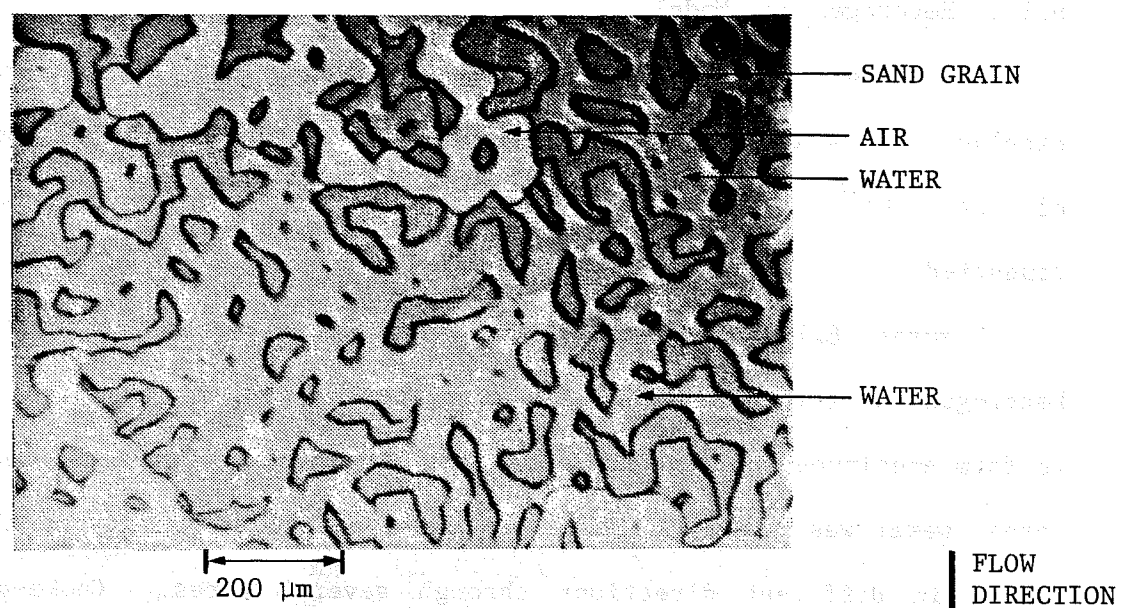

6.3a Early Stage of Displacement: Continuous Air Channel and Unswept Water Zones

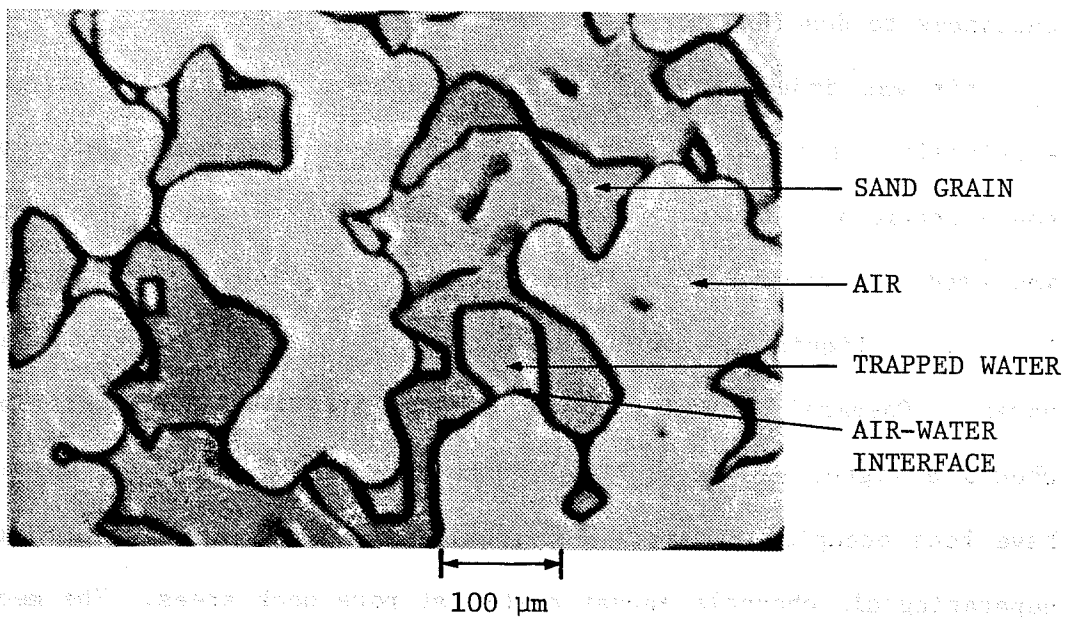

6.3b Air-Water Interface at Dead End Pore and Displacment Front

Fig. 6.3 AIR-WATER DISPLACEMENT: HETEROGENEOUS MODEL (OW.HET)

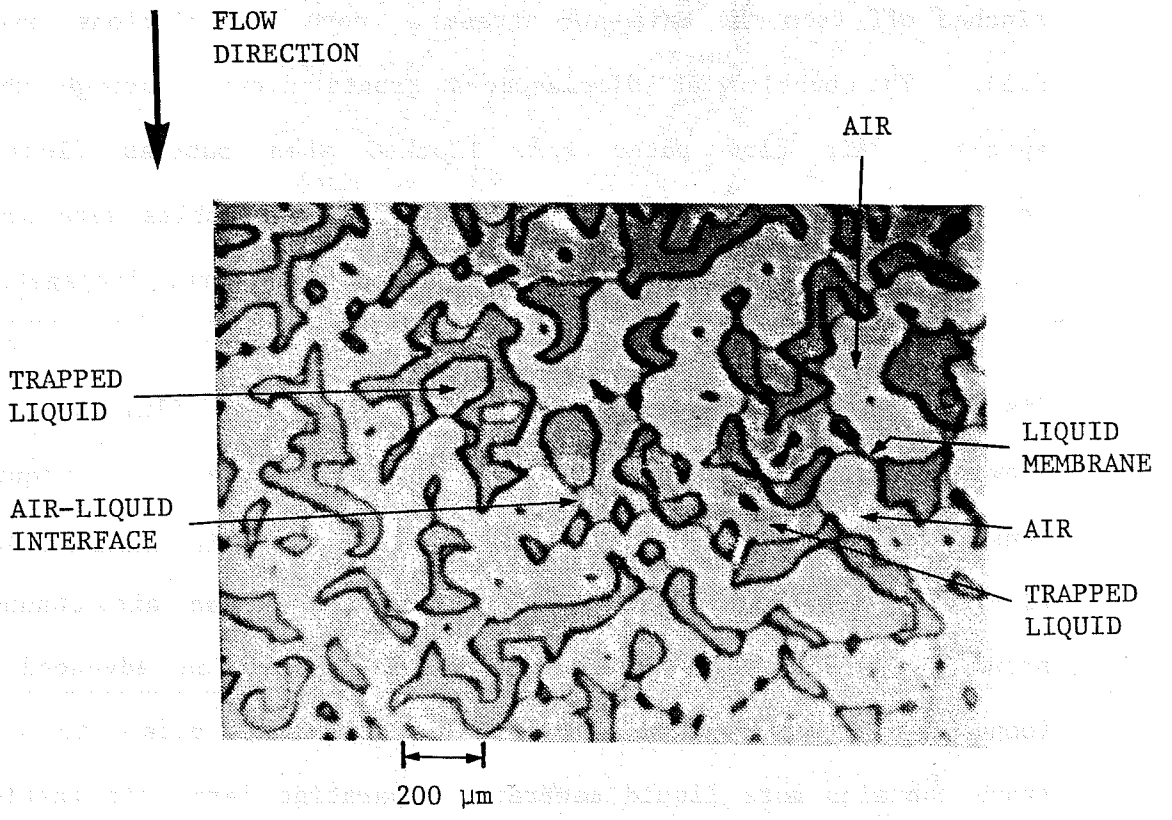

Fig. 6.4 FLUID DISTRIBUTION IN HETEROGENEOUS MODEL FOR 0.001% SURFACTANT CONCENTRATION

0.031% surfactant solution, foam bubbles were generated. Bubbles were formed by snap-off action, that is bubbles flowing into large pores were pinched off from the main air stream at pore constrictions (see Figs. 6.5). The bubbles at displacement fronts flowed through the pore spaces. Air flow paths were blocked when bubbles flowed into constricted pores. As shown in Figs. 6.5, the bubbles were sometimes trapped in dead end pores. The sequence of events, propagation and distribution of foam bubbles in the heterogeneous model will be discussed further in Section 7. The foam bubbles and fluid distribution shown in Figs. 6.5 are also typical of 0.124% surfactant concentration runs. In Fig. 6.5a, the locations of foam bubbles, liquid membranes, air-liquid interfaces, and the trailing end of an air channel are shown. In Fig. 6.5b, foam propagation is at an advanced stage. Compared to an intermediate stage of the flow (Fig. 6.5a), the advanced stage contains more liquid membranes separating large air bubbles. A typical polyhedral foam bubble is shown in Fig. 6.5b.

In the next section the effective air mobility found in the presence of water and in the presence of surfactant solution or foam will be presented.

6.2 EFFECTIVE AIR MOBILITY

Figure 6.6a is a typical pressure drop-time profile obtained during these experiments, and shows the range of pressure drops seen. The outlet pressure was kept at atmospheric pressure. In this particular run, air first entered the main body of the model at 2,100 seconds. Prior to this time, air was displacing the liquid in the entry headers. Breakthrough at the outlet occurred at 2,800 seconds. For the

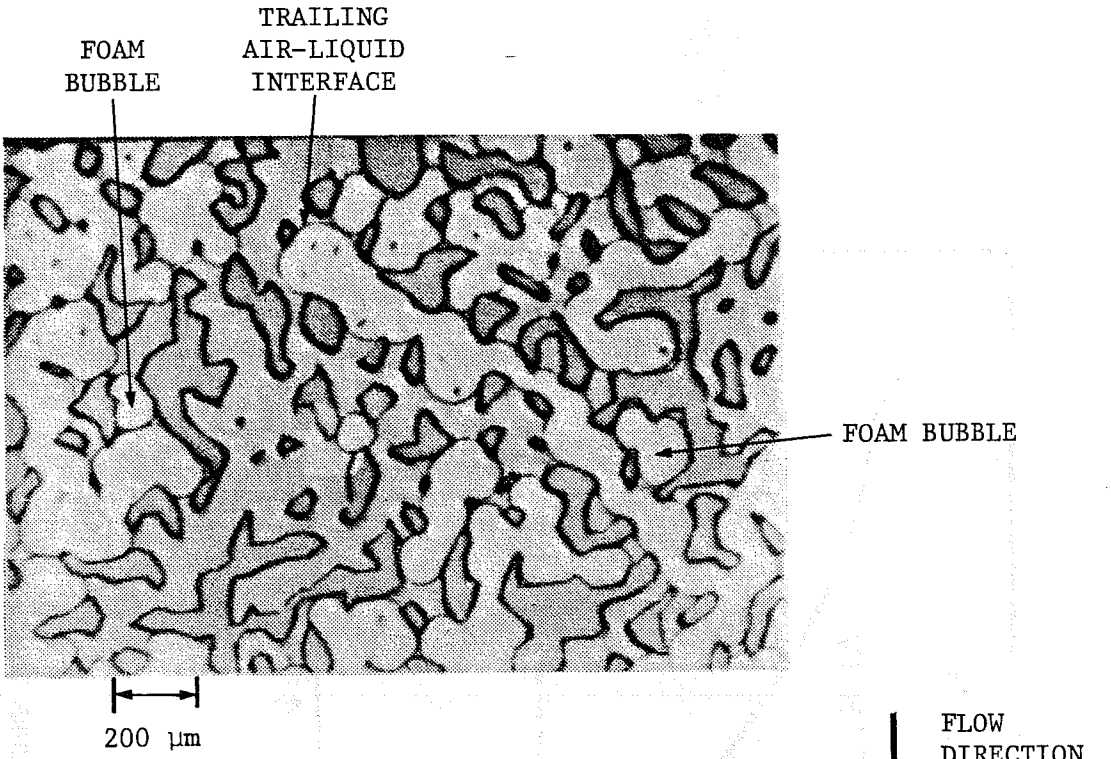

Fig. 6.5a Location of Foam Bubbles and Air-Liquid Interfaces

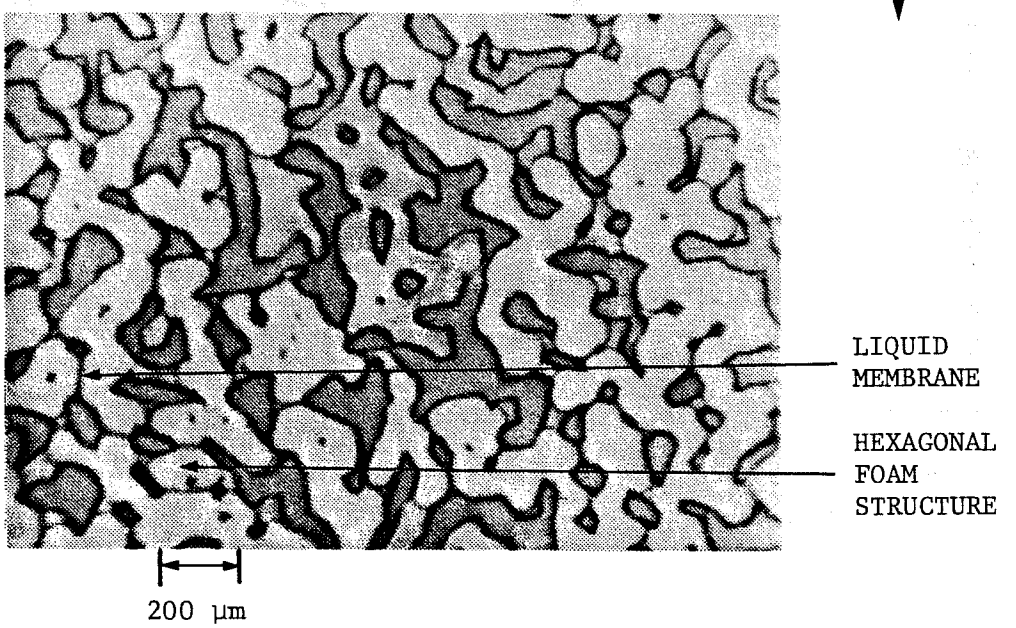

Fig. 6.5b Typical Polyhedral Foam Structure

Fig. 6.5 FOAM BUBBLES AND FLUID DISTRIBUTION IN HETEROGENEOUS MODEL FOR 0.031% SURFACTANT CONCENTRATION

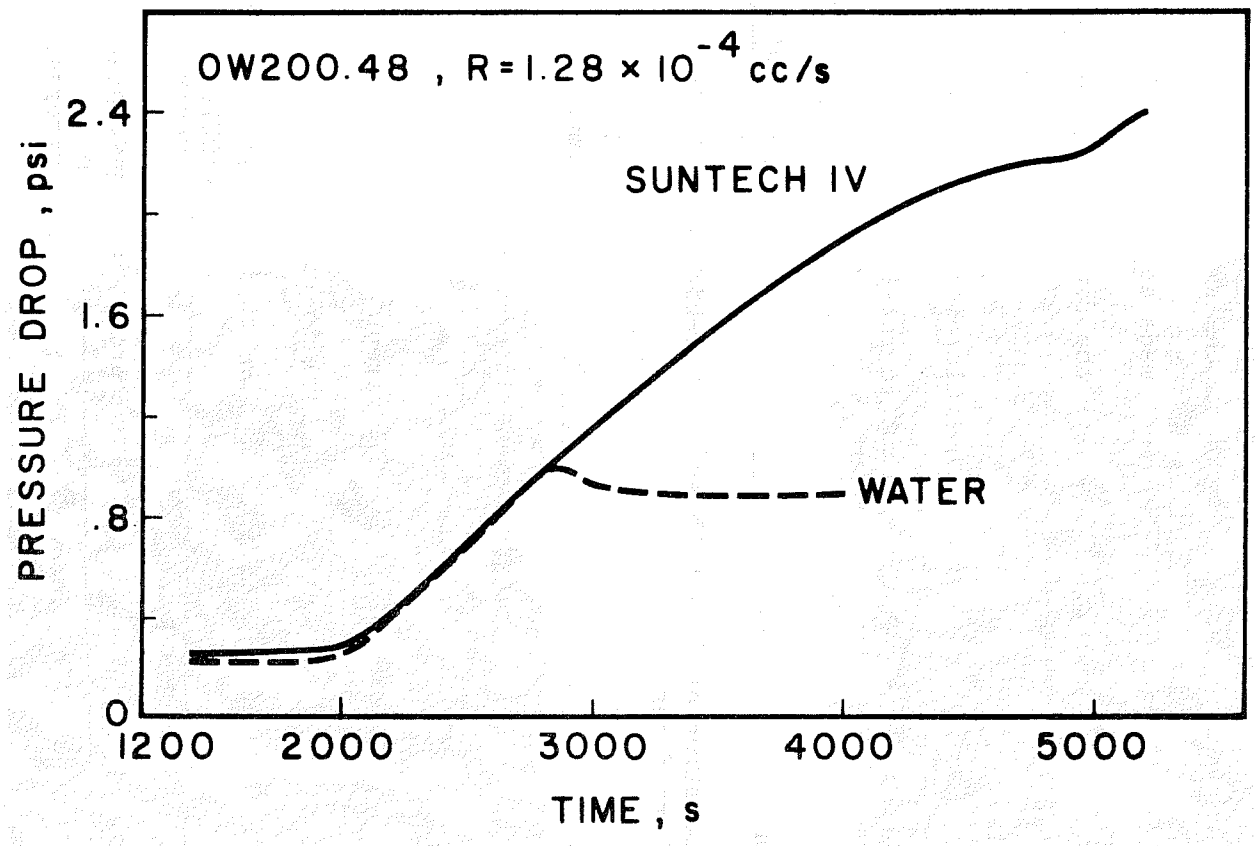

Fig. 6.6a TYPICAL PRESSURE DROP-TIME DATA

surfactant run, pressure continued to increase after air breakthrough.

From the basic data (such as shown in Fig. 6.6a), the volume of air injected at any given time is calculated. The pressure drop can be graphed versus the number of pore volumes of air injected, as shown in Fig. 6.6b. The greater pressure drop for the surfactant run (after gas breakthrough) is evident. Two water runs made at the same air injection rate are shown in Fig. 6.6b to illustrate the repeatability of the water runs.

When air is injected into the micromodel, the syringe pump displaces air at a constant pump volumetric rate. The air flowrate into the porous medium, however, changes with pressure drop. The air flowrate at model conditions was calculated as described in Section 5. Figure 6.6c displays the calculated air flowrate (at average pore pressure) in the porous medium as a function of cumulative air injected. The air flowrate of Fig. 6.6c is calculated using Eq. 5.5. As can be seen in Fig. 6.6c, the dashed line represents the pump rate, which is the average air flowrate during the experiment. Later on we refer to this as the nominal rate. Different pump rates were used for several experiments. To compute the effective air mobility, at any time, the air flowrate at that time and at that average pore pressure was used.

The effective air mobilities in the presence of water, surfactant solution, or foam are presented in both the homogeneous and heterogeneous micromodels in the following sections.

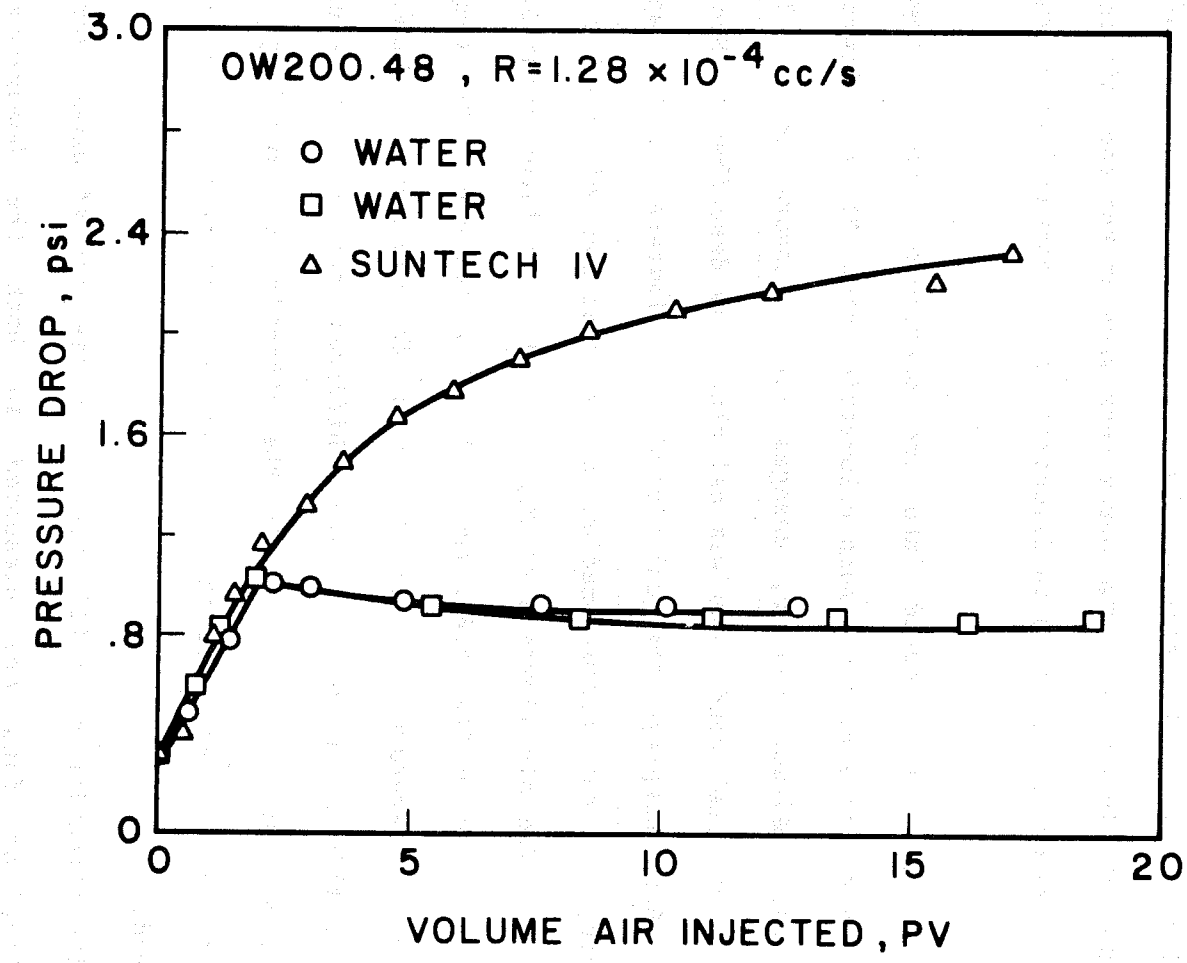

Fig. 6.6b PRESSURE DROPS vs CALCULATED AIR VOLUMES

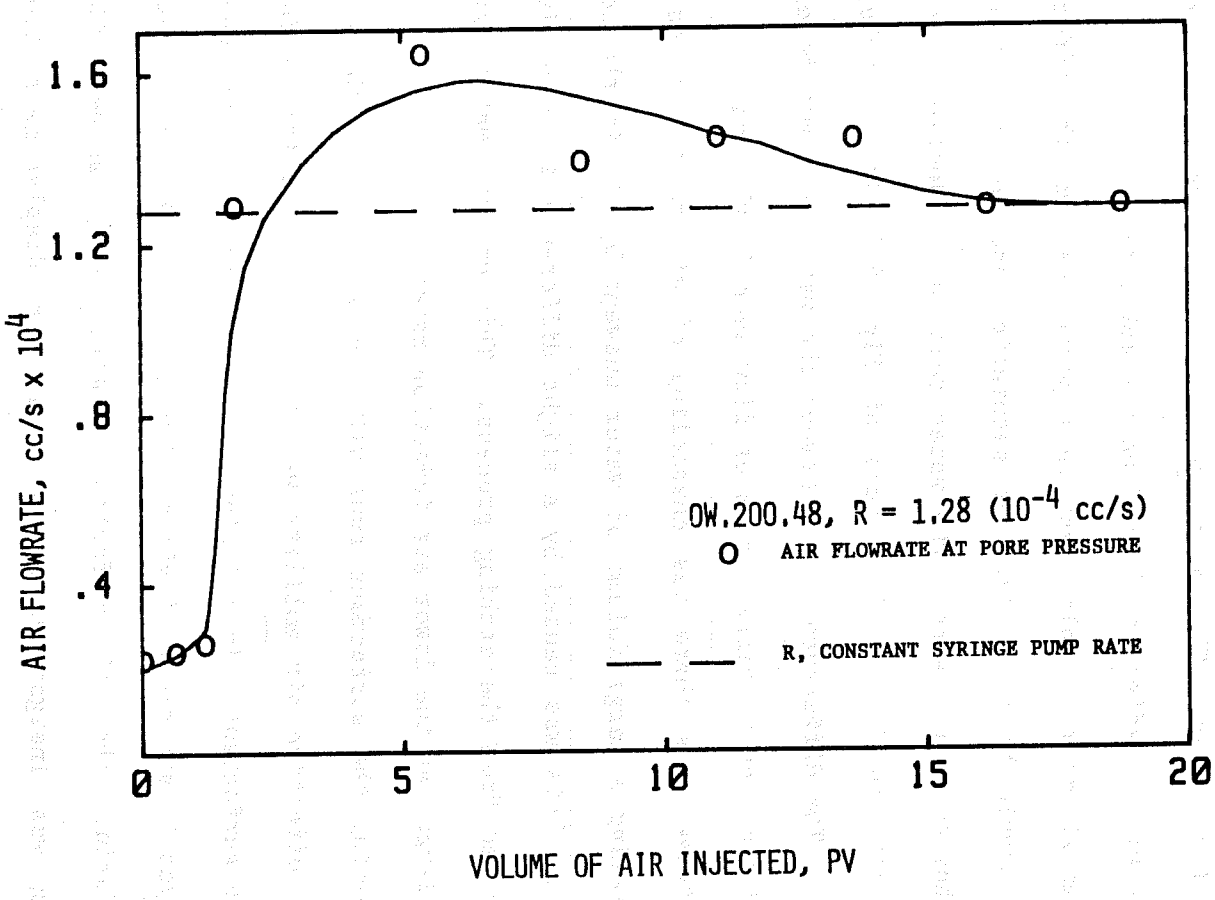

Fig. 6.6c AIR FLOWRATE AT AVERAGE PORE PRESSURE

6.2.1 Homogeneous Model

Figure 6.7 shows the effective air mobility plotted versus pore volumes of air injected for water and surfactant runs at various nominal air injection rates. The water runs were made to serve as a base case for comparing the effect of "foam" on air mobility.

In an air-water displacement in a porous medium, the effective air mobility should be a function of saturation and not of air injection rate. Thus one would expect the water runs (air injection rate of 2.56 x 10^{-4} cc/s and 1.92 x 10^{-4} cc/s of Fig. 6.7, for example) to be identical. The differences seen between the water runs may be explained by considering the preferred areas of flow seen in the model.

In these runs there was channeling of air to the sides of the model, leaving a large volume of water unswept by air in the center of the model. This was caused by a slight difference in pore dimensions that resulted from the etching process. This unswept water saturation zone was larger at the lower air injection rates.

Comparing the surfactant runs with the water runs (shown in Fig. 6.7), the effective air mobility was reduced by more than a factor of two by the surfactant. In addition, the surfactant runs show variations with changes in air rate. A visual observation of the swept area of the model, during the air-surfactant displacement, showed that air channeling was insignificant and a uniform displacement front was maintained. There was no unswept zone of the sort seen with the air-water runs.

Figure 6.8 shows the results obtained for model OW.200.48. The water runs follow the same trend as observed for model OW.200.20 (Fig. 6.7). The effective air mobility (water runs) also decreased with a

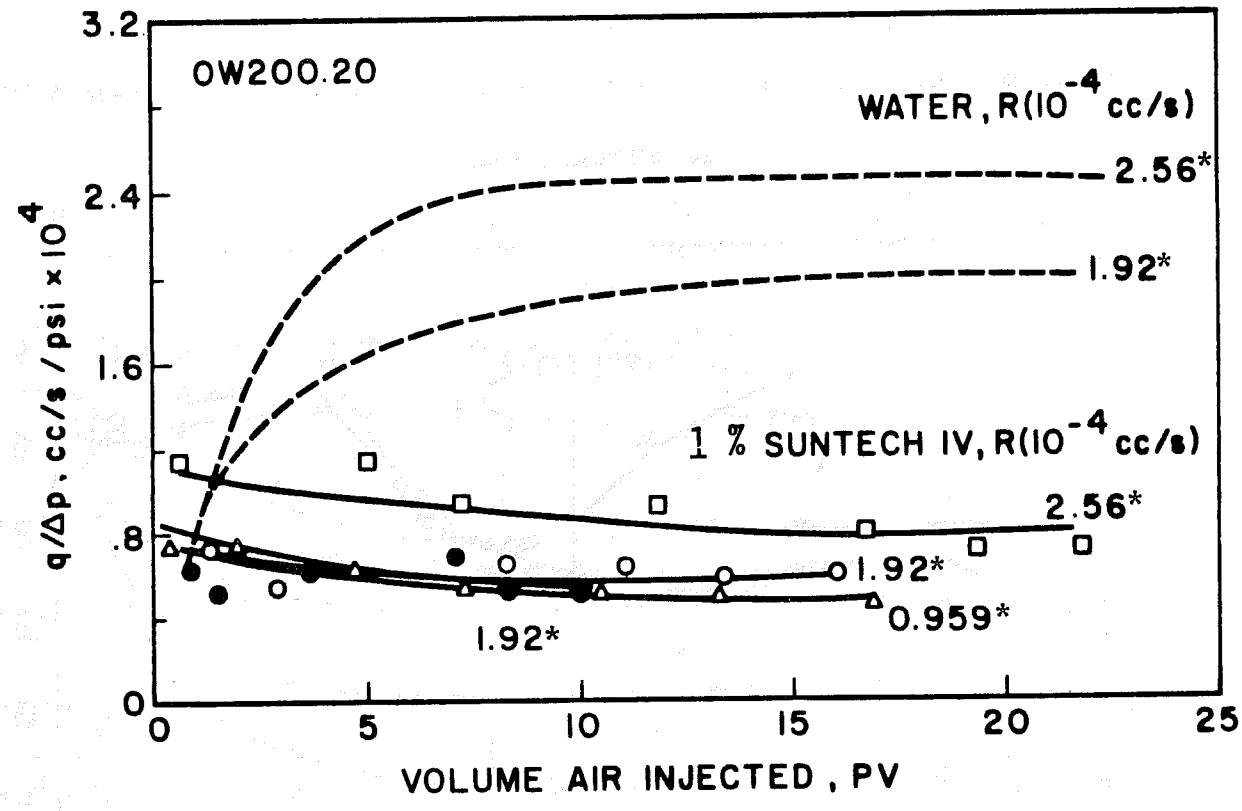

Note: * The number on each curve is the nominal flowrate [R]

Fig. 6.7 EFFECTIVE AIR MOBILITY AT VARIOUS NOMINAL AIR RATES: HOMOGENEOUS MODEL (OW.200.20)

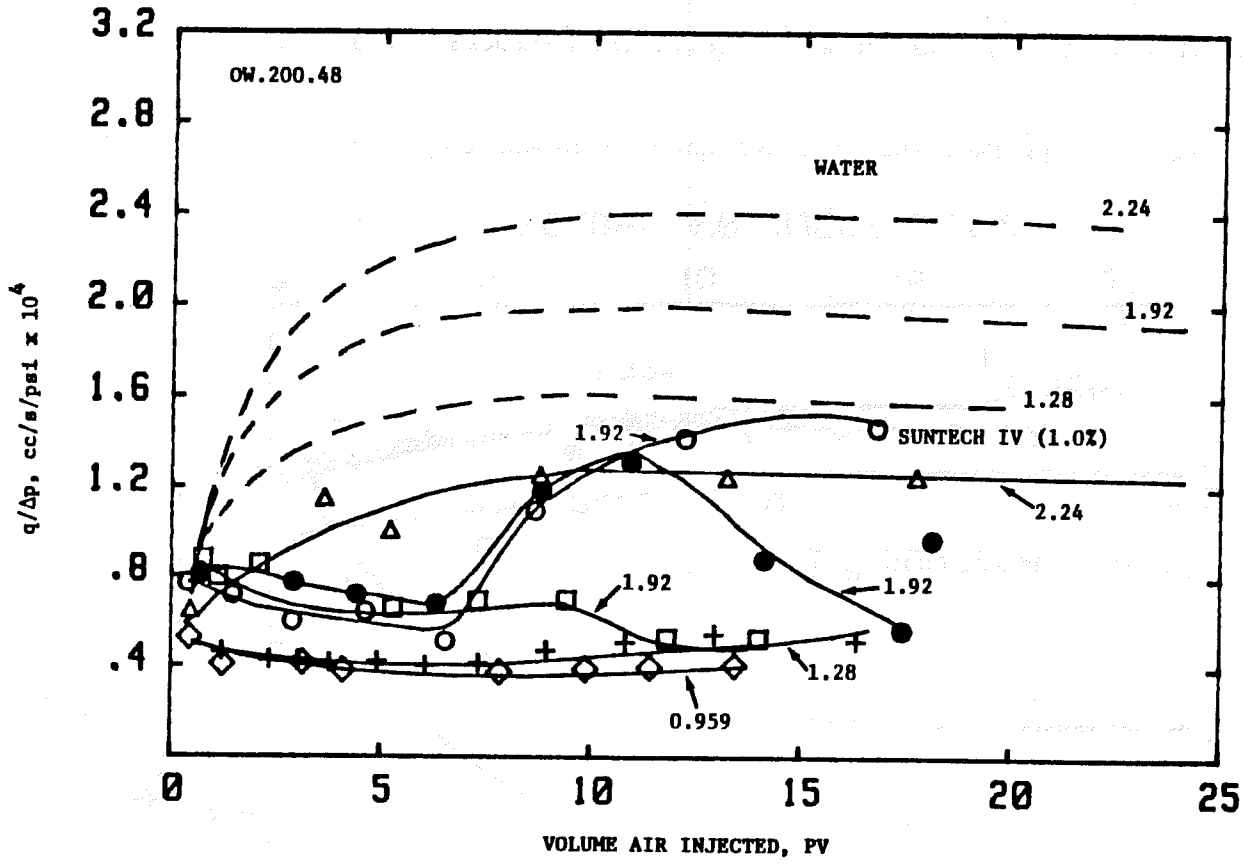

Fig. 6.8 EFFECTIVE AIR MOBILITY AT VARIOUS NOMINAL AIR RATES: HOMOGENEOUS MODEL (OW.200.48)

decrease in nominal air rate. The explanation given earlier for the variation of air mobility with nominal air rate (water runs of Fig. 6.7) also applied here.

A number of observations can be made about the surfactant runs in model OW.200.48 (Fig. 6.8). At low nominal air rates, the air mobilty shows a similar behavior as was observed in model OW.200.20 (Fig. 6.7). However, at an increased nominal air rate (1.92×10^{-4} cc/s) the data becomes erratic. After seven pore volumes of air injection the experiment was not reproducible, as seen in the three separate runs of the same rate. At a still higher rate, 2.24×10^{-4} cc/s, the effective air mobility shows a sudden rise and maintains the same general profile as in the water runs. The reasons for the observed variation in air mobility (for the surfactant runs of Fig. 6.8) were not known.

The third homogeneous model (OW.200.5) was used to study the effect of surfactant concentration on effective air mobility. Figure 6.9a shows that pressure drops across the porous medium were the same (within 10% experimental error) for surfactant concentrations ranging from 0.01 to 1%. At 0.001%, the pressure profile approaches that of water, however, there was still a reduction in air mobility. Figure 6.9b shows the effective air mobilities. At surfactant concentrations equal to and greater than 0.01%, effective air mobility was reduced (compared to an air-water displacement) by a factor of seven. Mobility reduction at 0.001% was by a factor of about 1.5.

The effect of surfactant concentration on effective air mobility in the presence of foam was also investigated with the heterogeneous model. These results are presented next.

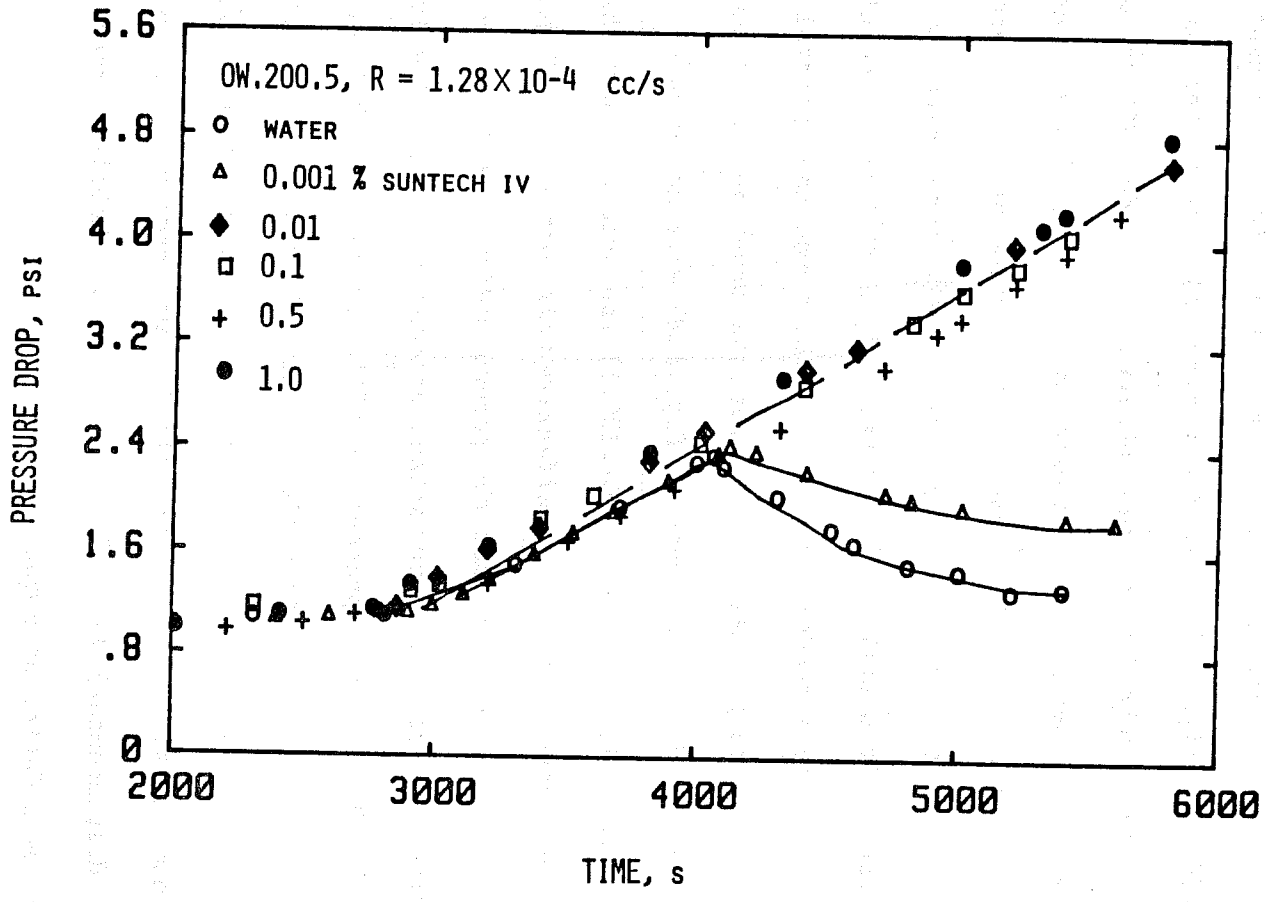

Fig. 6.9a PRESSURE DROP FOR VARIOUS SURFACTANT CONCENTRATIONS IN HOMOGENEOUS MODEL (OW.200.5)

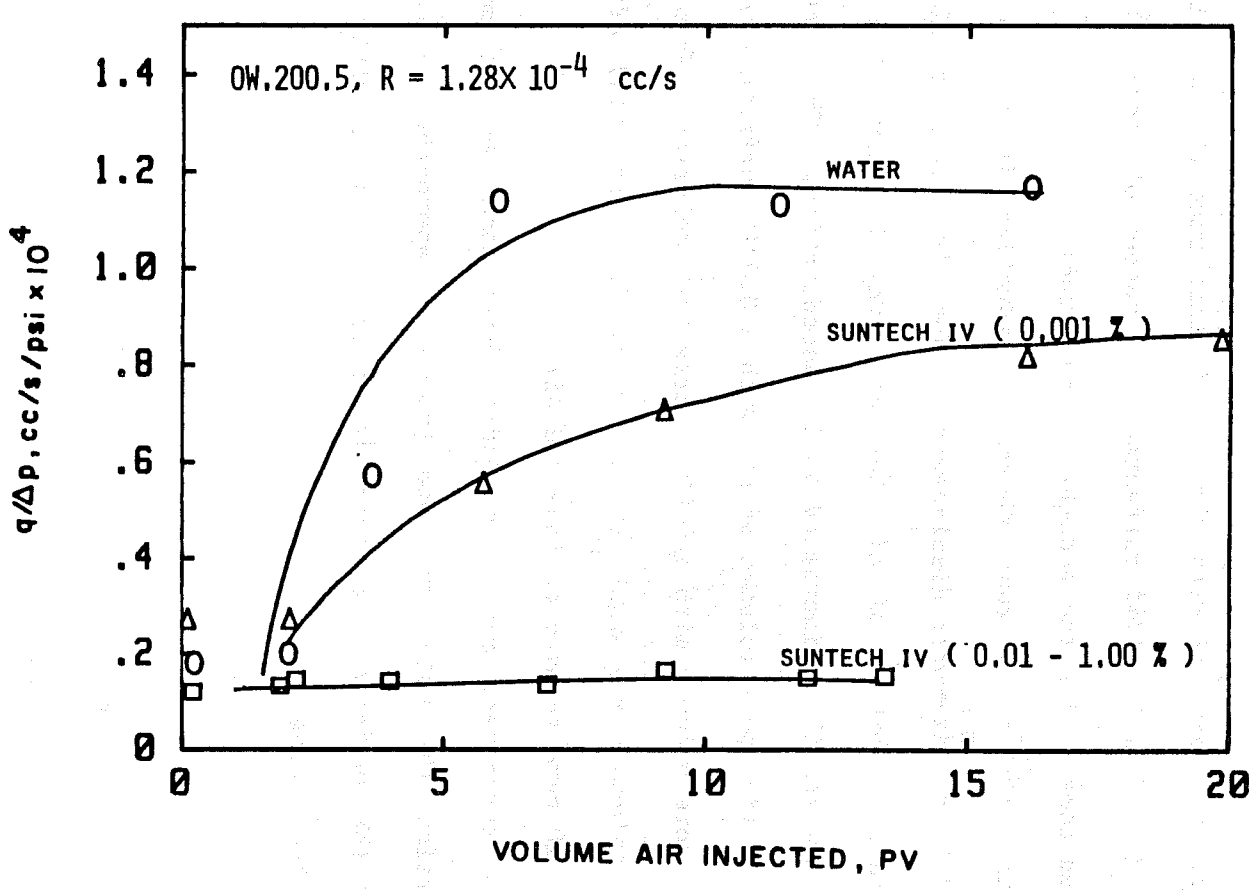

Fig. 6.9b EFFECTIVE AIR MOBILITY FOR VARIOUS SURFACTANT CONCENTRATIONS: HOMOGENEOUS MODEL (OW.200.5)

6.2.2 Heterogeneous Model

Figure 6.10 summarizes the results obtained with the heterogeneous model, OW.HET. Effective air mobility has been graphed as a function of volume of air injected into the porous medium. An air-water displacement was compared with three surfactant runs at concentrations of 0.001%, 0.031% and 0.124% surfactant. A number of observations can be made when considering the results of these runs.

All the surfactant runs showed a reduction in air mobility, compared with the air-water displacement. Foam effectiveness broke down after a certain volume of air has been injected into the porous medium. Foam stability increased with concentration. Thus, the foam broke down at five pore volumes of air with a 0.001% surfactant solution and at nine pore volumes with a 0.021% surfactant solution. When 0.124% surfactant solution was used, the generated foam was still effective (stable) at 20 pore volumes of injected air.

In the surfactant runs, even after breakdown, the air mobility remained below the water run and gradually approached a constant value. As the surfactant concentration increased the mobility at the constant value decreased.

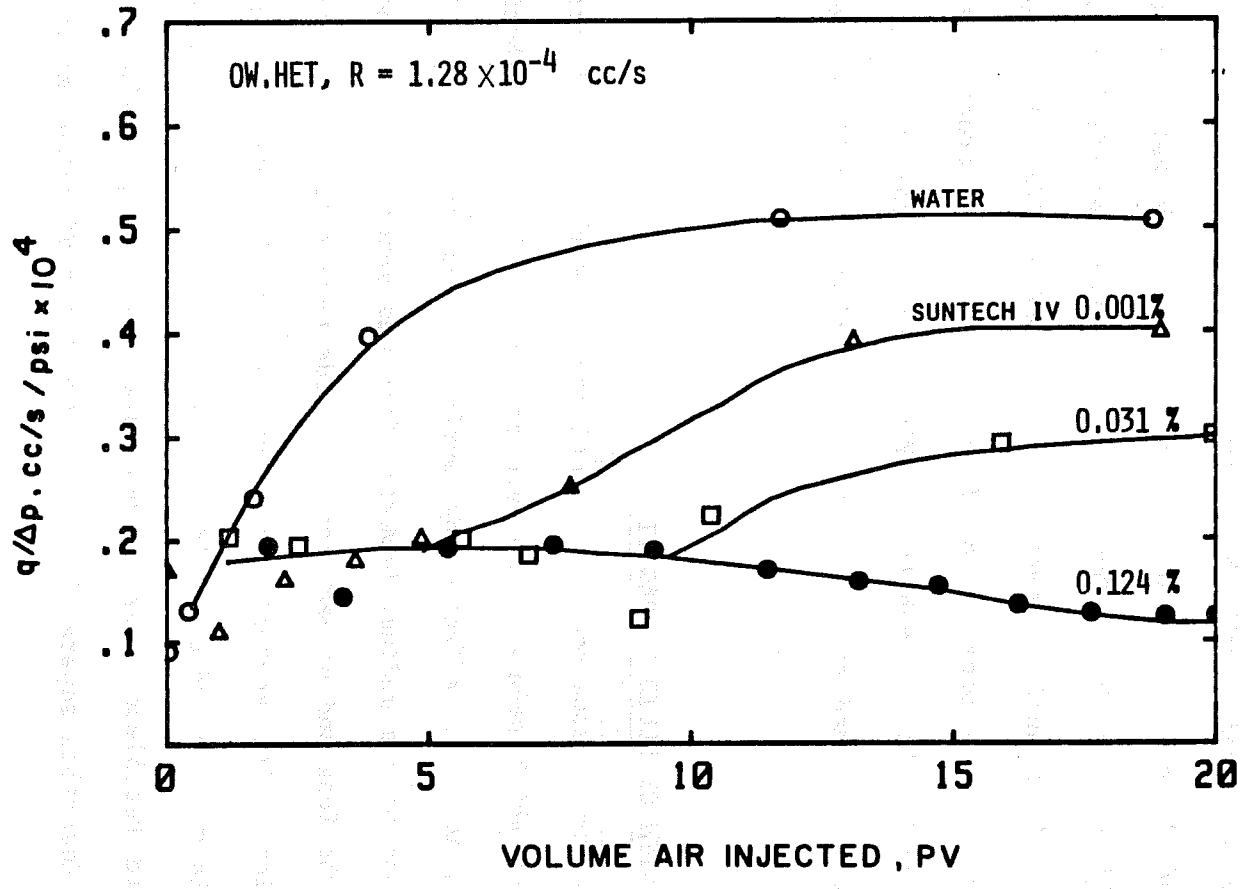

Fig. 6.10 EFFECTIVE AIR MOBILITY FOR VARIOUS SURFACTANT CONCENTRATIONS: HETEROGENEOUS MODEL (OW.HET)

7. DISCUSSION

In this section, the mechanism of fluid propagation in the homogeneous micromodels will be presented. Also, the formation of foam bubbles and the propapation of gas and liquid in the heterogeneous pore system will be described. Compared to the air-water displacement, the flow of air in a surfactant-filled porous medium (for the homogeneous models) and in the presence of foam (as in the heterogeneous model) caused reduction in air mobility. Fluid flow in the two pore systems will be compared, and explanations for the observed mobility reduction will be offered in this section.

7.1 MECHANISM OF FLUID PROPAGATION

In the homogeneous models, a continuous network of liquid membranes was observed which separated the air channels. Fluid distribution and propagation was not affected by surfactant concentration. In the heterogeneous porous medium, however, foam was actually generated. The nature of the foam and propagation of fluids were affected by surfactant concentration. The mechanism of fluid propagation observed in these porous media were recorded on video tapes. These tapes are available at the Stanford Petroleum Research Institute, Stanford , California. The mechanisms described separately for the two types of porous media used.

7.1.1 Mechanism of Fluid Propagation for the Homogeneous Model

Figure 7.1 depicts the observed flow mechanism. It shows the sequence of air and liquid movement that gives rise to the fluid configuration of Fig. 6.1.

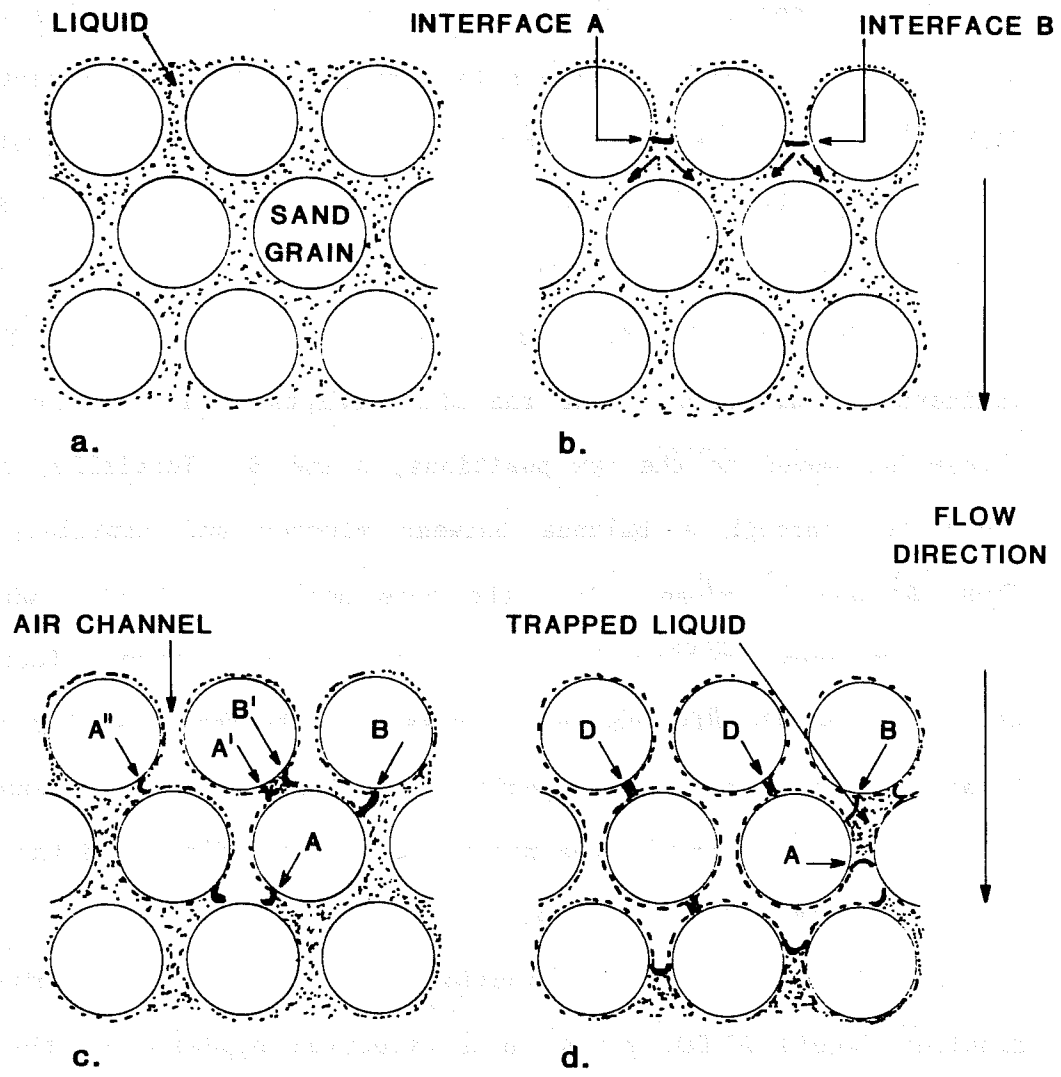

Fig. 7.1 MECHANISM OF FLUID PROPAGATION: HOMOGENEOUS MODEL

In Fig. 7.1a, the micromodel is fully saturated with aqueous surfactant solution. As air is injected into the model, Fig. 7.1b, air-liquid fronts (interfaces A and B for example) entering a pore body can flow into either of two adjacent pore necks as indicated by the short arrows. Many of the air fronts tend to go in the same direction, the right arrow for example, as shown in Fig. 7.1c for the two air-liquid fronts being considered. The choice of direction appears to be caused by the overall pressure distribution in the system.

The shape of air-liquid interfaces A^{11}, A^{1} and B^{1} in Fig. 7.1c indicate the directions that the air attempts to flow. The main air stream has moved to the new positions, A and B. Initially, the front propagates through a balance between viscous and capillary forces. Thus, A^{1} and B^{1} advance into the pore neck as indicated where they assume maximum curvature. Viscous forces become increasingly significant as the displacement progresses. The forces acting on A^{1} and B^{1} are, however, equal and opposite. The liquid trapped between A^{1} and B^{1} continues to drain via the network of liquid films, and the diagonal interfaces form as shown in Fig. 7.1d.

Occasionally, local distribution of pore pressures permits air to displace liquid a few pores in a direction opposite to the general flow. Such a movement is shown by the position of front A in Fig. 7.1d as compared to its position in Fig. 7.1c. These "backward" flows lead to trapping of liquid or air in some pores. Horizontal interfaces form when air is trapped.

The following section is devoted to fluid flow mechanism in the heterogeneous micromodel.

7.1.2 Heterogeneous Model

In this section, a mechanism of foam bubble formation and propagation in a heterogeneous pore network is described. Processes such as snap-off, trapping of air bubbles and liquid in dead-end pores, blocking of flow channels at pore constrictions by foam bubbles, and movement of fluid interfaces through pores have been observed and recorded on video tape. Figures 7.2a through 7.2c are photographs presented in the order they were taken during the experiment. In these figures the overall flow is from the top to the bottom.

Figure 7.2a shows a reference matrix grain (g), foam bubbles, b_2, b_3 and b_4 held between matrix grains, and a large air channel (a) with trailing edge (t). Adjacent to the large air channel is bubble b_1 confined by liquid membranes m_1 and m_2.

To understand the process of forming and propagating bubbles, a small area around trailing edge t, liquid membranes (m_1 and m_2) and bubble b_1 of Fig. 7.2a will be considered. Compare Figs. 7.2a and 7.2b in this overall area. Notice the large air bubble (air channel, a) has withdrawn its trailing edge (t) a pore distance in the time interval between the two figures.

The air channel, a, flows from the top left-hand corner of these figures 7.2 to the lower right-hand corner. In the time between Figs. 7.2b and 7.2c, liquid drains from the membrane (m_1) connecting b_1 and air channel (a). As the membrane (m_1) weakened, a and b_1 were eventually separated and the trailing edge (t) was propagated some distance in the flow direction. Notice how far it has moved in Fig. 7.2c. At an intermediate stage between Figs 7.2b and 7.2c, the leading membrane (m_1) advanced bubble b_1 into the large pore area (the area

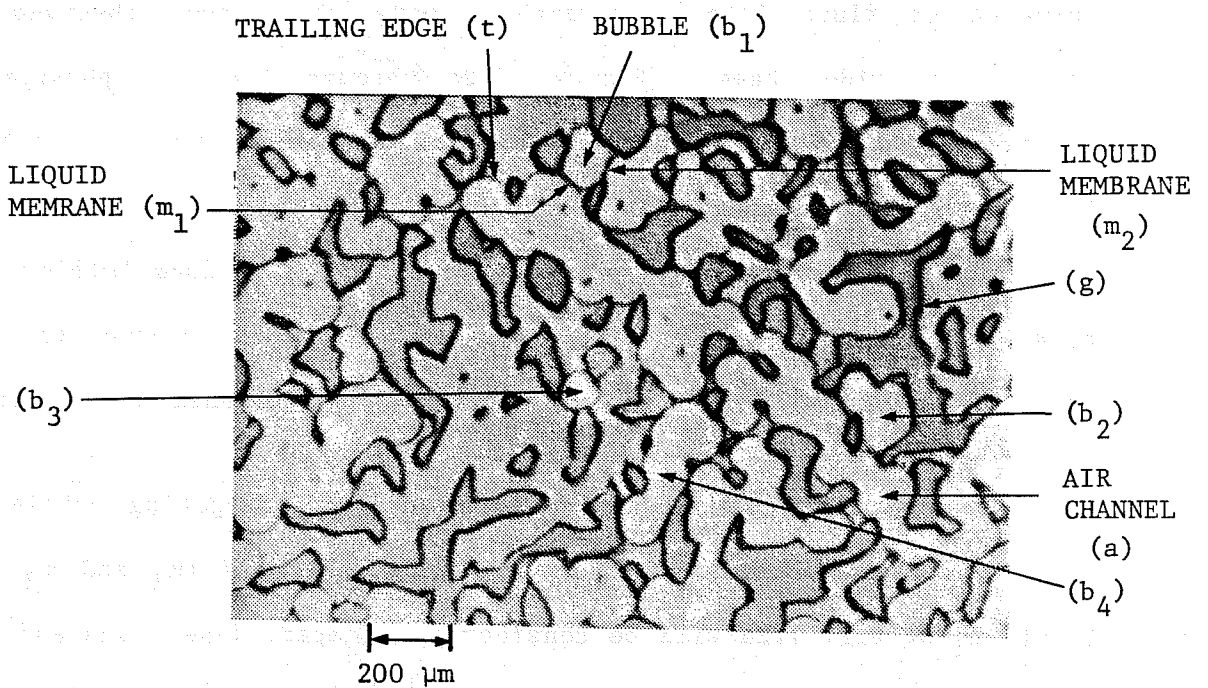

Fig. 7.2a Location of Bubbles and Membranes

Fig. 7.2 MECHANISM OF FOAM FORMATION AND FLUID PROPAGATION IN HETEROGENEOUS MODEL

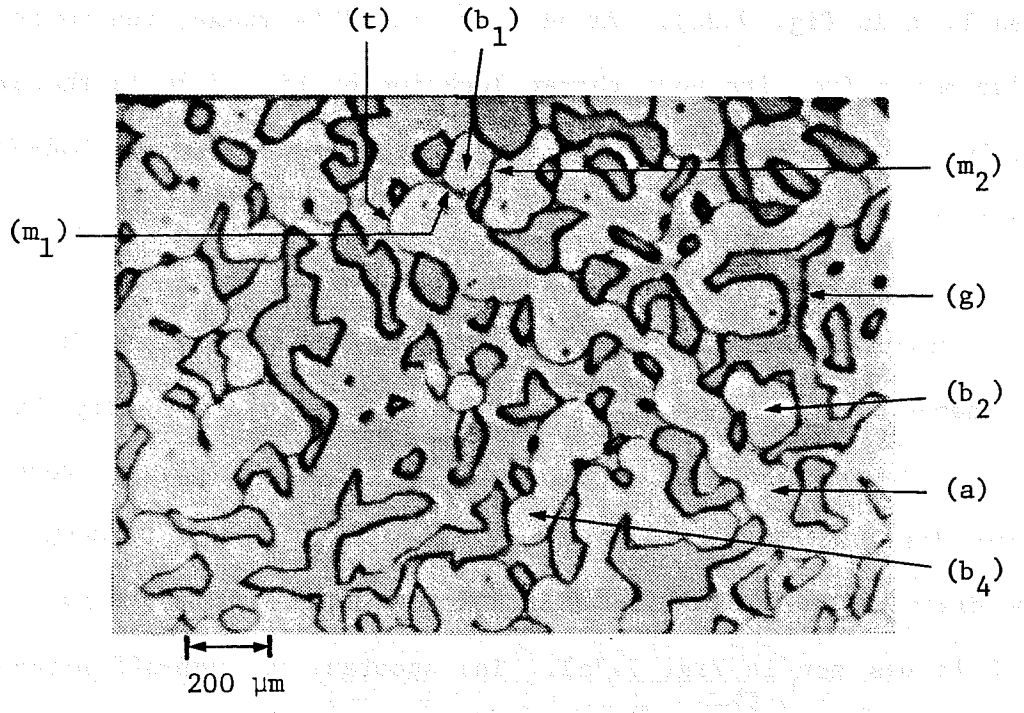

Fig. 7.2b Withdrawal of Fluid Interface from Pore

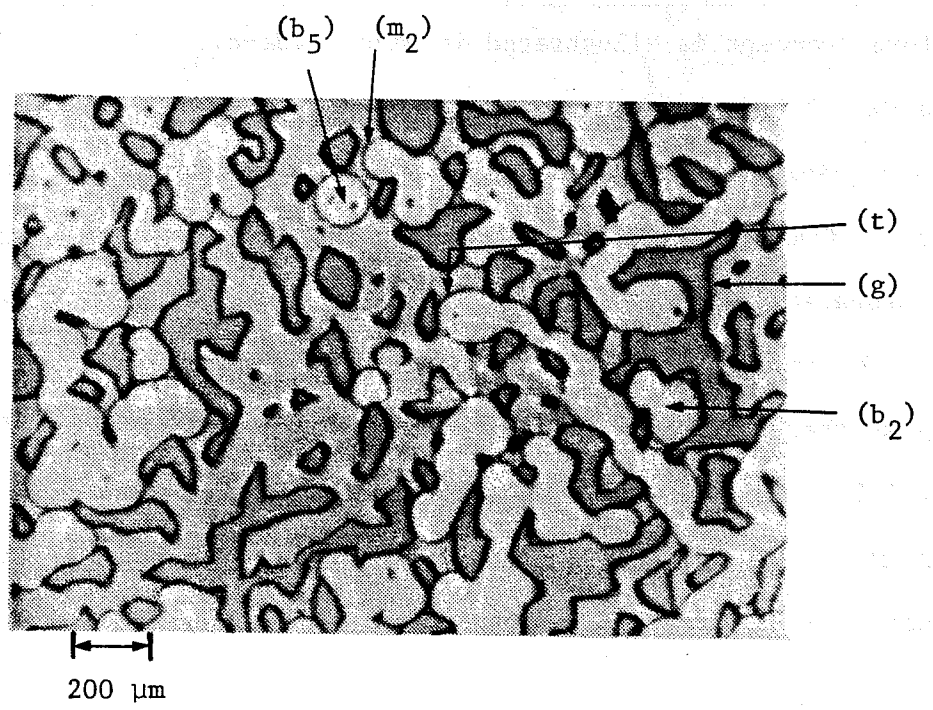

Fig. 7.2c Snap-off and Formation of Bubbles

occupied by t in Fig. 7.2c). At this intermediate stage, the membrane (m_2) also moved from its pore throat location of Fig. 7.2b to the area originally occupied by m_1. Since this was a favorable pore body-to-throat ratio, bubble b_1 snapped off at m_2 to give rise to bubble b_5 of Fig. 7.2c.

In general, in all displacement at high concentrations in this model, snap-off was observed at pore constrictions adjoining large pores. When snap-off takes place, the "parent bubble" recedes (withdraws its leading edge). Simultaneously, the snapped-off bubble is usually dislodged into a large pore and propagated through the pore system (it was not in Fig. 7.7c). The spontaneous snap-off process, withdrawal of fluid interfaces and dislodging of a new bubble from the parent air bubble are often described as "break and reform." The "break and reform" concept is illustrated in Figs. 7.3a-c.

In Fig. 7.3b, the displacing gas front of Figure 7.3a has advanced into an adjoining pore body. Snap-off occurs at the pore neck in Fig. 7.3c and a foam bubble is dislodged into the liquid. The foam bubble can be propagated through the pore system as shown by the arrow in Fig. 7.3c and the process of forming the foam bubble will repeat and continue as long as there is liquid in the pore area adjoining the gas front, as in Fig. 7.3a.

In the next section, a comparison of the flow mechanisms in the homogeneous and heterogeneous models is given.

7.1.3 Comparison of Flow Mechanisms

Fluid flow behavior in the micromodel will be discussed in relation to the pore structures and the fluids used for the experiments. First,

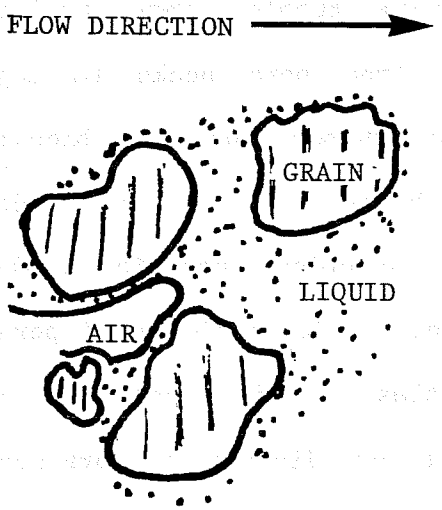

FIG. 7.3a Air Bubble at Pore Neck

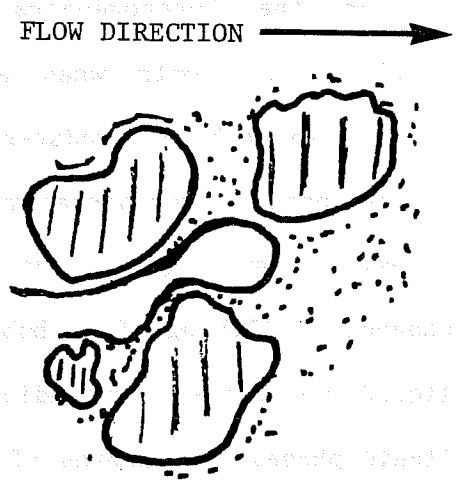

Fig. 7.3b Bubble Advances to Adjoining Bore Body Area

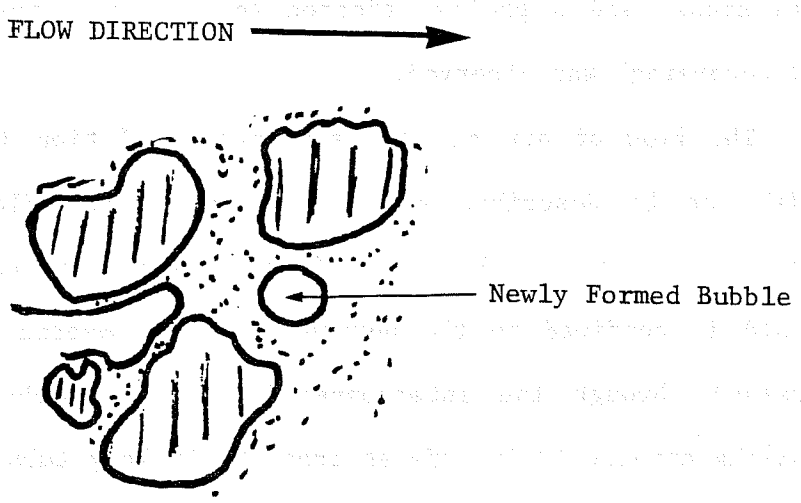

Fig. 7.3c Snap-off (Formation of Bubble)

Fig. 7.3 BUBBLE "BREAK AND REFORM" PROCESS

a summary of fluid distribution and flow in the heterogeneous model is given.

In the heterogeneous model, foam bubbles were produced at displacement fronts when air flowed from pore necks to adjoining pores. The bubbles produced flowed through pore channels, blocking the narrow ones. Occasionally, small bubbles were trapped in dead-end pores. Liquid (water or surfactant solution) occupied small pore channels. Although foam bubbles trapped liquid in the small pores, the liquid membranes surrounding the bubbles provided continuity of the liquid phase. The shapes of the bubbles were dictated by pore geometry, absence or presence of other bubbles and the relative strength of the capillary and viscous forces. Bubble size was a function of surfactant concentration. At high surfactant concentrations, small foam bubbles were obtained. Snap-off occurred at pore constrictions adjoining large pore areas, and a process rferred to (in the literature) as "breaking and reforming" was observed.

The flow of air and the surfactant solution in the homogeneous model can be described as a modified channel flow. The air flows through the pores in channels defined by a network of liquid films. The liquid is confined to the periphery of the matrix grains and it flows (drains) through the interconnecting liquid membranes. Leading and trailing air-liquid interfaces trap air in long tubular bubbles. As the enclosed air flows between the pores, the interfaces change curvature (they deform rather than break) and continously assume shapes dictated by the pore geometry. Liquid and air are trapped in some pores when two or more leading fronts flow in directions counter to each other.

The characteristic polyhedral bubbles with nearly straight edges that constitute foams, as described by Bikerman (1973) and observed in the heterogeneous model, were not produced in the homogeneous models. In the homogeneous model, bubbles smaller than two pore diameters rarely formed, and "breaking and reforming" of foam bubbles was not characteristic of the flow phenomenon. Rather, air was propagated in tubular bubbles moving and extending across several pores. Air-liquid interfaces deformed to assume shapes dictated by the pore geometry, interfacial intension and pressure forces.

Both the homogeneous and heterogeneous models were highly water-wet because of the silicon dioxide matrix surface. The wettability is evident from the fluid distribution in Fig. 6.1. Thus, the air displacement experiment is that of a non-wetting phase displacing a wetting phase (aqueous surfactant solution).

The absence of polyhedral foam bubbles and "break and reform" mechanism in the homogeneous models can be explained from the work done by Roof (1970) and Mohanty, et al. (1980). They investigated the conditions that must be met in order for snap-off to occur in a water-wet system. The criterium for snap-off to occur in a flow channel is for the leading fluid interface to advance into pore bodies considerably larger than the throats. In the homogeneous models, leading fluid interfaces are constrained by matrix grains on the downstream side before the curvature can expand enough to cause snap-off at the upstream pore-neck.

In the following section, reasons for the reduction in effect of air mobility will be considered.

7.2 EFFECTIVE AIR MOBILITY

Results on the mobility of air in the presence of foams and in an air-water displacement were presented in Section 6. Foam acted as a mobility-reducing agent. Large mobility reduction factors were obtained. Mobility reduction factor is the ratio of air mobility in an air-water system to the air mobility in air-foam (or surfactant) system. Considering the stable cases, low air injection rates and high surfactant concentrations, the results of Section 6 show reduction factors of 7.7, 3.3, 3.5 and 4.2 for models OW.200.5, OW.200.20, OW.200.48 and OW.HET, respectively. These reduction factors are plotted versus the absolute permeability of the micromodels as shown in Fig. 7.4. Mobility reduction decreased to a constant value with absolute permeability. Bernard and Holm (1964) reported an increase in mobility reduction factor with absolute permeability. It should be noted, however, that Bernard and Holm used different porous media than used here (sand packs and consolidated cores). They also generated foam in-situ by simultaneously injecting liquid and gas into the porous medium. The results of the homogeneous and heterogeneous micromodels were plotted on the same graph (Fig. 7.4) only because they correlate.

Causes of mobility reduction in the micromodels will now be discussed.

Non-uniformity in the shape and distribution of matrix grains in the heterogenous model resulted in a system of randomly distributed large, small and dead-end pores. Pore constriction and a few grain contacts exist in the heterogeneous model. When foam formed, some pores were blocked by bubbles. Blocking took place at pore constrictions. The bubbles also blocked the entrance to dead-end pores. Air is

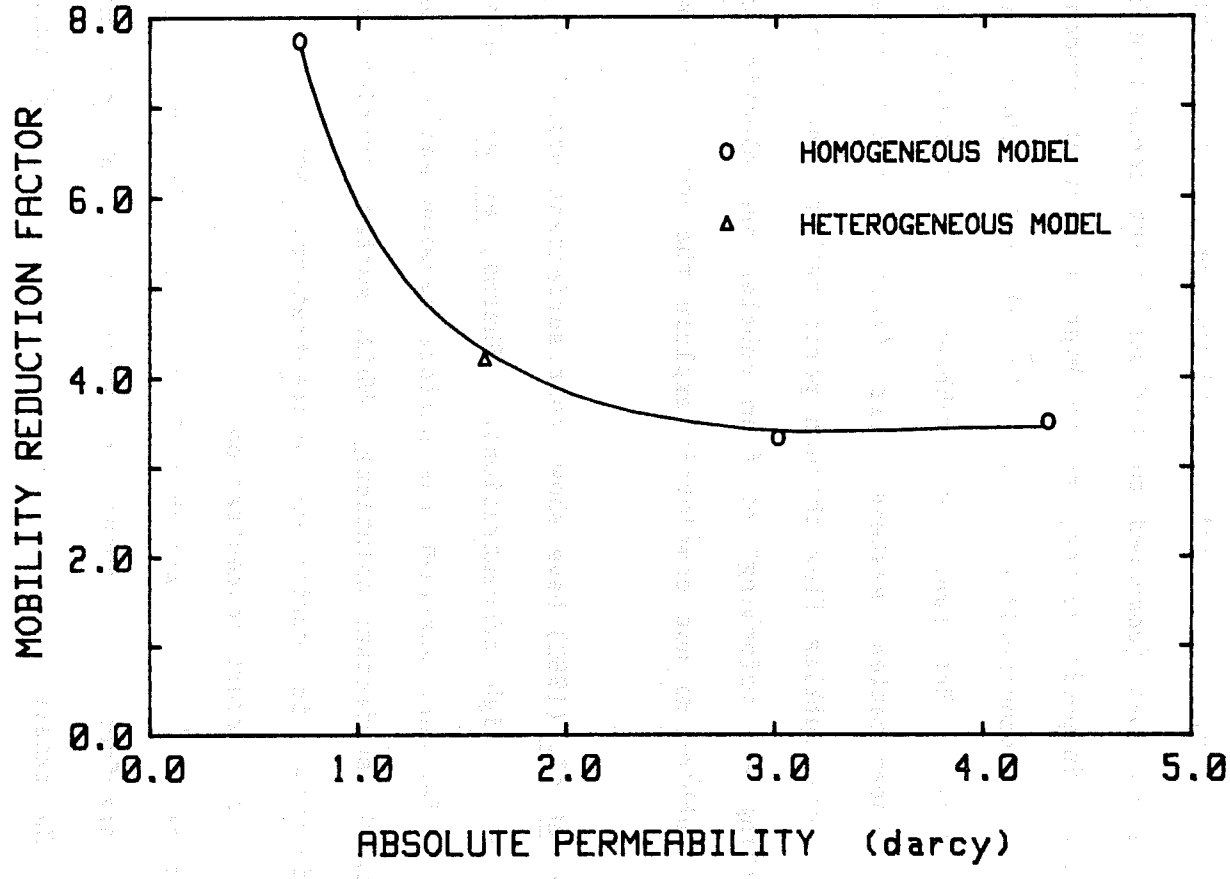

Fig. 7.4 MOBILITY REDUCTION IN THE PRESENCE OF SURFACTANT vs ABSOLUTE PERMEABILITY

propagated in large bubbles through channels. When air experiences sudden pressure drops in adjoining large pores, bubbles "break and reform". The resulting effect is a temporary break in the continuity of air channels.

High surfactant concentrations produced small foam bubbles and caused more reductions (compared to low surfactant concentrations) in air mobility. Snap-off action, as in high surfactant concentration systems, causes discontinuities in air channels and produces reduction in air mobility. But small air bubbles, characteristic of high surfactant concentration systems, aid (rather than impede) air propagation: more bubbles flow through pores rather than block pores. Thus, "breaking and reforming" of foam bubbles and blocking of flow channels by bubbles do not completely explain the process of mobility reduction.

Sharma, et al. (1982) have shown that surfactant solutions produce small bubbles at high concentrations. Sharma, et al., using also Suntech IV surfactant, measured the surface tension and surface shear viscosity of the surfactant solutions. While surface tension decreased with an increase in surfactant concentration, surface viscosity increased with surfactant concentration.

The interaction between air channels and liquid film network at the air-liquid interfaces is another possible cause of air mobility reduction. The existence of high surface viscosity at high surfactant concentrations partially explains the mobility reductions obtained in the homogeneous system. In the homogeneous micromodels, "true" foam bubbles were not generated; instead, a continuous network of air channels and liquid membranes existed. High surface viscosity would

give the liquid membranes extra strength to resist the flow of air. High surface viscosity implies that the concentration of molecules is greater at the air-liquid interface.

Trapped liquid and air also reduce the effective mobility of injected air. The results of this study were presented in Section 6 and discussed in this section. A summary of this work will be given in the following.

8. CONCLUSIONS

Micromodels were used to simulate a monolayer of both homogeneous and heterogeneous porous media. The mechanism of propagation of foam and its components (air and surfactant solution) was visually studied and recorded on video tapes. These video tapes are available at the Stanford University Petroleum Research Institute, Stanford, California.

The displacement of aqueous surfactant solution by air in the homogeneous porous media can be described as modified channel flow. The liquid forms a network of interconnecting films around the matrix grains and between pores. Air was propagated in channels consisting of tubular bubbles flowing and extending across several pore lengths. Liquid and air were trapped in some pores. Foam, consisting of polyhedral bubbles or other characteristic structure was not generated, nor was "breaking and reforming" of foam bubbles observed.

Membranes, that is, air-liquid interfaces, were propagated through homogeneous the porous media. These interfaces change their curvature (assuming shapes dictated by pore geometry) as they move through the pore system.

Three homogeneous micromodels with differing pore dimensions were used for this study. Pore dimension did not affect the observed flow mechanism.

In the heterogeneous porous medium, true foam was generated at high surfactant concentration. Both spherical and polyhedral foam bubbles were produced. Large bubbles took shapes dictated by pore geometry. Liquid flowed through small pores while maintaining a continuous network through the foam liquid membranes. Pore structure influenced the flow

process. Snap-off occurred at pore constrictions, and the resulting foam bubble "break and reform" process was observed. Trapping of liquid and air bubbles and blocking of pore channels by bubbles were functions of the pore geometry. Propagation of membranes, similar to the mechanism in the homogeneous models, was observed.

A considerable reduction of effective air mobility was observed in the presence of foam, compared to air-water systems without surfactant. Mobility reduction was dependent on flow mechanisms. Flow mechanism and air mobility were not significantly affected by air injection rates in the range studied.

Effective air mobility decreased with an increase in surfactant concentration in both the homogeneous and heterogeneous porous media. Beyond a certain concentration, however, mobility reduction converged to one value regardless of concentration changes. In the heterogeneous porous medium, surfactant concentration affected the flow mechanism. Foam bubbles produced with high surfactant concentrations were smaller than those generated in low surfactant concentrations.

9. RECOMMENDATIONS

A commercially prepared foaming agent, Suntech IV, was used for this study. The purity and composition of different Suntech IV batches differed. It is recommended that further fundamental work on foam flow behavior be done with pure surfactants such as sodium dodecyl sulfate ($C_{12}H_{25}SO_4Na$), and other heterogeneous models similar to OW.HET. The following areas of work are recommended.

9.1 MECHANISM OF FOAM PROPAGATION

Observe the mechanism(s) of foam propagation at low and high surfactant concentrations. Relate the mechanisms to the surfactant's surface properties such as surface tension and surface viscosity. Small and mobile foam bubbles may be generated at high surfactant concentrations. At low surfactant concentrations (low surface viscosity and high surface tension), membrane propagation (movement of fluid interfaces) may be dominant. This should be determined.

In either type of propagation, capillary forces would be expected to be dominant and capillary equilibrium would be expected as flow progresses. Thus, there should be a study of capillary forces, measured by membrane curvatures, to see if they are the same at different "islands", i.e., clusters of sand grains connected by air-liquid membranes and enclosing unswept (uninvaded) liquid portions.

9.2 PHASE PREFERENCE OF FOAM

Determine which phase, oil or aqueous, that gas (air or nitrogen) preferentially reacts with during foam formation and propagation.

Saturate a micromodel with aqueous surfactant solution and some light oil. Inject air or nitrogen and observe where and how it propagates in the model.

9.3 MIXED FOAMING SYSTEMS

Working with mixed foaming systems, sodium lauryl sulfate and alcohols ($C_{12}H_{25}SO_4Na$ + $C_nH_{2n+1}OH$), Sharma, et al. (Jan. 1982) found that surface properties of foaming solutions and microscopic characteristics of foam show a correlation with the flow behavior of foam in porous media. The bubble size distribution of static foam was one of the characteristcs correlated.

It is recommended that the foaming systems (sodium lauryl sulfate and alcohols) used by Sharma, et al. (Jan. 1982) be used in the micromodel experiments. A correlation of the displacement behavior, such as air mobility, mechanism of foam propagation and bubble size distribution in the micromodel, with the reported flow behavior could have a far reaching implication. It might be possible to select foaming systems based on their surface properties and microscopic characteristics of static foams.

9.4 HETEROGENEOUS-HOMOGENEOUS POROUS MICROMODEL

A micromodel consisting of two different pore structures arranged in some pre-determined fashion should be fabricated. Each pore structure would be homogeneous and each would be etched into specified areas of the model. A visual study of foam simultaneosly flowing through each homogeneous section would shed light on the influence of pore structure on foam flow behavior.

NOMENCLATURE

a, b, d, ℓ = the external dimensions of the micromodel flow areas, cm.

D = grain diameter (base)

f = grain diameter (top)

h = the etched depth of the model, cm

k_d = absolute permeability of micromodel, millidarcies

n = pore neck (spacing between grains)

p = pore body diameter

p_a = atmospheric pressure, psia

p_l = inlet pressure, psia

p_s = initial syringe pressure, psia

$\bar{p}$ = average pore pressure, psia

$\bar{p}_l$ = average inlet pressure, psia

Q_a = cumulative volume of air injected into the model (evaluated at atmospheric pressure), cc

$\bar{Q}$ = average cumulative volume of air injected, evaluated at pore pressure, cc

Q_{aE} = Cumulative volume of air (at atmospheric pressure) injected into the headers at time, t_E, cc

q = fluid flowrate, cc/s

q_a = air flowrate (at atmospheric pressure), cc/s

$\bar{q}$ = air flowrate at pore pressure, cc/s

R = constant, nominal syringe pump rate, cc/s

r_b = pore body radius

r_t = pore throat radius

t = time, sec

t_E = time at which air first enters the porous medium, sec

V_p = dimensionless pore volume of the micromodel

V_s = initial volume of air in the syringe, cc

Δp = total pressure drop across the model, psi

ϕ = porosity of micromodel, fraction

μ = viscosity of the flowing fluid, c_p

REFERENCES

1. Albrecht, R. A., and Marsden, S. S., "Foams as Blocking Agents in Porous Media," Soc. Pet. Eng. J. (March, 1970), 31.

2. Bernard, G. G., and Holm, L. W., "Effect of Foam on Permeability of Porous Media to Gas," Soc. Pet. Eng. J. (Sept. 1964), 267.

3. Bernard, G. G., Holm, L.W. and Jacobs, W.1., "Effect of Foam on Trapped Gas Saturation and on the Permeability of Porous Media to Water," Trans. AIME, (1965), 234, 295.

4. Bikerman, J. J., Foams, Springer-Verlag New York Inc., 1973.

5. Bonnet, J., "Study of Multiphase Flow in Porous Media," Ph.D. Thesis, Toulouse University, Toulouse, France, 1978.

6. David, A., and Marsden, S. S., "The Rheology of Foam," SPE 2544 presented at the 44th Annual Fall Meeting of Soc. of Pet. Eng. of AIME, Denver, Colo., Sept. 28-Oct. 1, 1969.

7. Davis, J. A., and Jones, S. C., "Displacement Mechanisms of Miccellar Solutions," J. Pet. Tech. (Dec. 1968), 1415.

8. Deming, J. R., "Fundamental Properties of Foams and their Effects on the Efficiency of the Foam-Drive Process,"

M.S. Thesis, Pet. & Nat. Gas. Eng., Penn. State Univ. (Dec. 1964)

9. Egbogah, E. O., and Dawe, R. A., "Microvisual Studies of Size Distribution of Oil Droplets in Porous Media," Bulletin of Canadian Petroleum Geology, 28, No. 2 (June 1980), 200-210.

10. Elson, T. D., "The Effectiveness of Foaming Agents at Elevated Temperatures over an Extended Period of Time," M. S. Report, Pet. Eng., Stanford University, 1979.

11. Fried, A. N., "The Foam Drive Process for Increasing the Recovery of Oil," U.S. Bureau of Mines, R.I. 5866 (1961).

12. Gardescu, I. I., "Behavior of Gas Bubbles in Capillary Spaces," Trans. AIME, (1930), 86, 351-370.

13. Handy, L. L., Amaefule, J. O., and Ziegler, V. M., "Thermal Stability of Surfactants for Reservoir Application," SPE 7867, presented at the SPE of AIME International Symposium on Oilfield and Geothermal Chemistry, Houston, Texas, Jan. 22-24, 1979.

14. Holbrook, S. T., John, T. P., and Hsu, W., "Rheology of Mobility Control Foams," SPE/DOE 9809, presented at the 1981 SPE/DOE Second Joint Symposium on Enhanced Oil Recovery of the Soc. of Pet. Eng., Tulsa, Oklahoma, April 5-8, 1981.

15. Holcomb, D. L., "Foamed Hydrocarbon Stimulatiom of Water Sensitive Formations," SPE 9033 presented at the SPE Rocky Mountain Regional Meeting, Casper, Wyoming, May 14-16, 1980,

16. Holcomb, D. L., Callaway, E., and Curry L.: "Chemistry, Physical Nature and Rheology of an Aqueous Stimulation Foam," Soc. Pet. Eng. J. (Aug. 1981), 410-414

17. Holm, L. W., "The Mechanism of Gas and Liquid Flow through Porous Media in the Presence of Foam," Soc. Pet. Eng. J. (Dec. 1968), 359

18. Holm, L. W., "Foam Injection Test in the Siggins Field, Illinois," J. Pet. Tech. (Dec., 1970), 1499

19. Ikoku, C. U., "Transient Flow of Non-Newtonian Power-Law Fluids in Porous Media," Ph.D. Thesis, Petroleum Engineering Dept., Stanford University,1978.

20. Jones, S. C., Marathon Oil Co.: Notes on etched glass micromodels, contained in a letter to O. S. Owete, May 1980.

21. Kander, M., and Schechter, R. S., "On the Mechanism of Foam Formation in Porous Media," SPE 6200, presented at the 51st Annual Fall Meeting of Soc. of Pet. Eng. of AIME, New Orleans, La., Oct. 3-6, 1976.

22. Kolb, G. E., "Several Factors Affecting the Foam-Drive Process for the Removal of Water from Consolidated Porous Media," M.S. Degree Thesis, Pet. & Nat. Gas Eng., Penn. State Univ. (Dec. 1964).

23. Malmberg, W. E., Burtch, W. F.: "Large-Scale Samples of Sulfonates for Laboratory Studies in Tertiary Oil Recovery, Preparation and Related Studies," Final Report, FE-2605-20, Prepared for the US Department of Energy, May, 1979.

24. Marsden, S. S., Jr., and Khan, S. A., "The Flow of Foam through Short Porous Media and Apparent Viscosity Measurements," Soc. Pet. Eng. J. (Mar. 1966), 17.

25. Marsden, S. S., Jr., Elson, T., and Guppy, K., "Literature Review of the Selected Blockage of Fluids in Thermal Recovery Projects," TR-3, Stanford University Petroleum Research Institute, Stanford, California, (Nov. 1977)

26. Marsden, S. S., Jr., "Non-Newtonian Fluids," Class notes for Petroleum Engineering 284, Stanford University, 1979.

27. Mast, R. F., "Microscopic Behavior of Foam in Porous Media," SPE 3997 presented at the 47th Annual Fall Meeting of the Soc. of Pet. Eng. of AIME, San Antonio, Texas, Oct. 1972.

28. Mattax, C. C., and Kyte, J. R., "Ever See A Water Flood?," Oil and Gas J. (Oct. 16, 1961), 115.

29. Minssieux, L., "Oil Displacement by Foams in Relation to Their Physical Properties in Porous Media," J. Pet. Tech. (Jan. 1974), 100.

30. Mohanty, K. K., Davies, H. T., and Scriven, L. E., "Physics of Oil Entrapment in Water-Wet Rock," SPE 9406, presented at the 55th Annual Fall Meeting of the SPE of AIME, Dallas, Texas, Sept. 21-24, 1980.

31. Nahid, B. H., "Non-Darcy Flow of Gas through Porous Media in the Presence of Surface Active Agents," Ph.D. Thesis, University of Southern California, Los Angeles, 1971.

32. Owete, S. O., et al., "Foam as a Mobility Control Agent in Steam Injection Processes--Temperature Stability of Foaming Agents; Application to Improved Steam Injection," SPE 8912-B, presented at the 50th Annual California Regional Meeting, Pasadena, California, April 9-11, 1980.

33. Pomerantz, D. I., "Anodic Bonding," U.S. Patent #3397278, Aug. 1968.

34. Raza, S. H., "Foam in Porous Media: Characteristics and Potential Applications," Soc. Pet. Eng. J. (Dec. 1970), 328.

35. Raza, S. H., and Marsden, S. S., "The Streaming Potential and Rheology of Foam," Soc. Pet. Eng. J. (Dec. 1967), 359.

36. Reid, V. W., Longman, G. F. and Heinerth, E., "Determination of Anionic-Active Detergents by Two-Phase Titration," Tenside 4, (1967), 292-304.

37. Roof, J.G., "Snap-Off of Oil Droplets in Water-Wet Pores," Soc. Pet. Eng. J. (March 1970), Pp 85-90.

38. Sharma, S.K., "A Study of the Microscopic Behavior of the Foam Drive Method," M.S. Report, Stanford University, Dec. 1965.

39. Sharma, M. K., Shah, D. O., and Brigham, W. E., "The Chain Length Compatibility and Surface Properties of Foaming Solutions in Relation to Fluid Displacement Efficiency in Porous Media," SPE 10612, presented at the SPE 6th. International Symposium on Oil Field and Geothermal Chemistry, Dallas, Texas, Jan.1982

40. Sharma, M. K., Shah, D. O., and Brigham, W. E., "A Correlation of Surface and Microscopic Properties of Foaming Agents in Relation to Fluid Displacement Efficiency in Porous Media," Paper submitted for publication, Canad. J. Pet. Tech., (1982). Original paper available at the Dept. of Chemical Engr., University of Florida, Gainesville, Florida.

41. Terry, C. S., "A Gas Chromatography System Fabricated on a Silicon Wafer Using Integrated Circuit Technology," Technical Report No. 4603-1, SEL-75-011, Integrated Circuits Laboratories, Stanford University, May 1975.

42. Wallis, G., and Pomerantz, D. I., "Field Assisted Glass-Metal Sealing," J. Amer. Ceram. Soc., 40, (1969), 3946-3849,

43. Wardlaw, N. C., "The Influence of Pore Structure in Rocks on the Entrapment of Oil," Canadian Society of Petroleum Geologists, Jan. 1980.

44. Wardlaw, N. C., and Cassan, J. P., "Estimation of Recovery Efficiency by Visual Observation of Pore Systems in Reservoir Rocks: Reply, "Bulletin of Canadian Petroleum Geology, 27, No. 3 (Sept. 1979), 402-404.

APPENDIX A

MICROMODEL FABRICATION

The fabrication of the micromodel consists of three steps: microprocessing, anodic bonding and attachment of tubes. In the microprocessing stage a design of the porous medium is transferred by means of a photomask on to an oxidized silicon wafer. A chemical etching technique is used to produce the desired porous matrix. To seal the porous medium, a glass plate is anodically bonded to the etched silicon wafer. Finally, tubes for fluid injection and production are attached to the model. The three processes will be described separately.

A.1 MICROPROCESSING

For the homogeneous micromodel, a design of the pore geometry and the overall fluid flow pattern was made. Figure A.1 shows this pattern. The desired pore spacing (to be obtained after etching) was determined and an appropriate design was prepared. A master drawing of the flow pattern (including the detailed pore system) was produced in four separate reticules using a pattern generator. A photomask of each reticule was then made from the master drawing with a reduction factor of ten. An art design, "Formatt No. 7149", was used for the heterogenous porous medium. Formatt No. 7149 is a pre-generated pattern manufactured by Graphic Coorporation and sold in art shops. A sheet was cut from the pattern in the shape of the fluid flow pattern of Fig. A.1, but was eight times bigger than the actual size. By photo reduction,

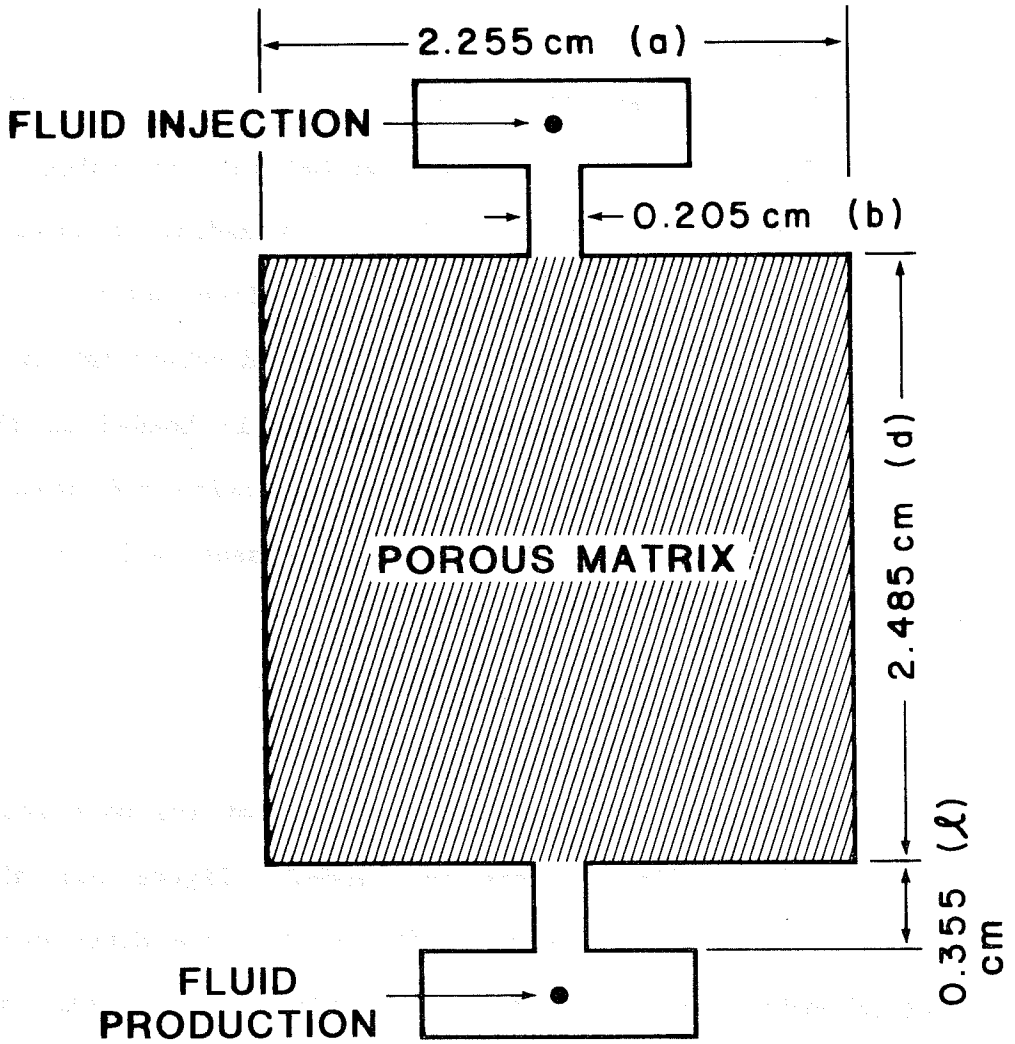

Fig. A.1 FLUID FLOW PATTERN

the actual size of the flow pattern was achieved and the pattern's pore size automatically reduced to dimensions near those of real porous media.

The starting material for the micromodel fabrication is a silicon wafer, 5 cm. in diameter, of medium resistivity (greater than 0.1 Ohm-cm) and polished on one side. The silicon wafer was prepared for oxidization in the following manner:

a. Rinse in de-ionized (DI) H_2O , 1 minute.

b. Soak in 1 part H_2SO_4 : 1 part H_2O_2 , heated, 10 minutes.

c. Rinse in DI H_2O , 3 minutes.

d. Soak in 5 parts H_2O : 1 part H_2O_2 : 1 part NH_4OH , heated, 10 minutes.

e. Rinse in DI H_2O , 3 minutes.

f. Dip 30 seconds in 10 parts H_2O : 1 part HF.

g. Rinse 5 minutes in DI H_2O.

h. Blow dry in nitrogen (filtered to 0.8 microns).

The wafer was then oxidized by passing streams of oxygen: dry oxygen for 10 minutes, wet oxygen (oxygen bubbled through water) for 3 hours and dry oxygen at 1250 ^{o}C for 10 minutes.

In the next step, the pattern to be etched was imprinted on the oxidized silicon wafer by a photographic process. A negative photoresist, Kodak KTFR, was spun onto the wafer and the photomask (prepared earlier) was positioned on the wafer. The photoresist was then exposed for approximately seven seconds to ultraviolet light (UV) through the photomask. (A negative photoresist polymerizes on exposure to UV light, positive photoresist loses its polymerization on exposure to UV light. The necessary polarity of the mask depends on the

photoresist type used.) The photoresist was developed by rinsing unpolymerized photoresist off the wafer.

After exposing and developing the photoresist, a hydrofluoric acid etch (6 parts NH_4F : 1 part HF) was used to remove oxide in exposed areas of the wafer.

Chemical etching was done in HF : HNO_3 mixture (10% HF, 90% HNO_3, concentrated reagents). The solution was agitated gently. Exposed silicon wafer areas etch downward and sideways at about the same rate, leaving sloping walls with a slope approximately 45 degrees. In the heterogenous model, the walls had a slope of 54.7 degrees. The remaining oxide was stripped in hydrofluoric acid. NOTE: 15 angstroms of "native oxide" will immediately grow on the silicon wafer surface in air at room temperature.

The etched silicon wafer has to be sealed at the top so that an enclosed porous medium is obtained. The method used is outlined in the next section.

A.2 ANODIC BONDING OF GLASS TO SILICON

Given the pore dimensions of the micromodel, an efficient means of fluid injection and production was required. Also, air flow must be confined to the pore spaces and prevented from "riding" above the sand grains. The fluid flow area was sealed with glass irreversibly bonded to the etched surface of the silicon.

Corning glass #7740, 5 x 5 cm and optically flat on one side was used for the bonding. Two holes, each 1 mm in diameter, were drilled (using a diamond drill) on the glass to match the fluid injection and production points of the etched silicon wafer shown in Fig. A.1. The wafer and the glass were degreased in solvents as follows:

a. Washed in soap solution and placed in ultrasonic cleaner.

b. Rinsed in distilled water.

c. Soaked in 1,1,1 trichloroethane for 15 minutes

d. Washed in acetone.

The polished surfaces of the silicon and the glass were placed together, and electrodes were held against their outer surfaces. Figure A.2 shows the arrangement. The temperature of this system was raised to about 400°C on a hot plate. A 600 volt potential was then applied between the electrodes with the silicon held positive with respect to the glass. The electric potential between the silicon and the glass pulls them into close contact and they bond immediately.

The development of electrostatic attraction between the glass and silicon wafer is described by Terry (1975) as follows:
"At elevated temperatures (yet below the 700°C softening point of the pyrex), the positive sodium ions in the glass become quite mobile. They are attracted to the negative electrode on the glass surface where they are neutralized. The more permanently bound negative ions in the glass are left, forming a space charge layer in the glass adjacent to the silicon surface. The time-varying potential distribution is shown in Fig. A.3 (Fig. A1.2 of Terry's text) as a function of position in the glass plate. After the Na^+ have drifted toward the cathode, most of the potential drop in the glass occurs at the surface next to the silicon. The two wafers (the glass and the silicon) then act as a parallel plate capacitor with most of the 600 V potential being dropped across the several micron wide air gap between them. The resulting high E-field between the surfaces serves to pull them into contact with a force of 25 Kg/cm^2.

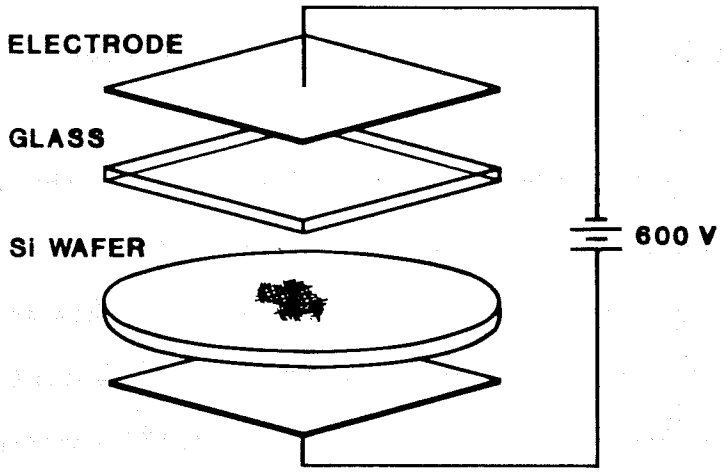

Fig. A.2 SCHEMATIC OF ANODIC BONDING PROCESS

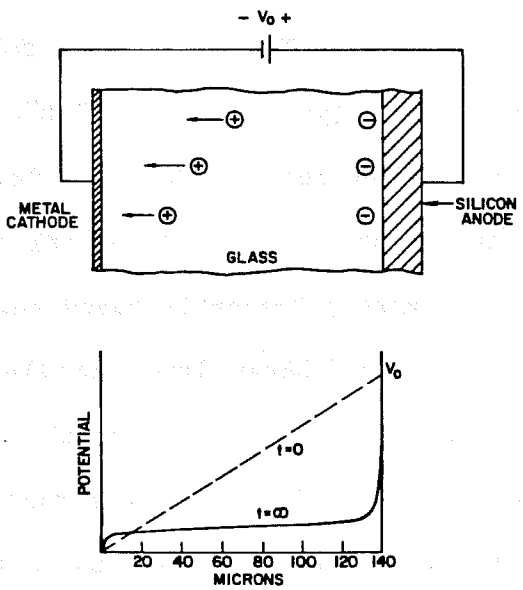

Fig. A.3 INITIAL AND FINAL EQUILIBRIUM DC POTENTIAL DISTRIBUTIONS ACROSS THE CORNING GLASS DURING ANODIC BONDING

"Once the wafers are in contact, almost all of the 600 V potential is dropped across the space charge layer in the glass. The extremely high fields which develop in that region transport oxygen out of the glass to bond with the silicon surface. The seal appears to be chemical in nature, similar to a fusion bond, except that the temperatures necessary for silicon-glass fusion are never reached."

The procedure is simple and easy to carry out. There are no fillers between the silicon wafer and the glass plate. Thus, fluid flow in the model is confined to the pore channels. In addition, the quality of the bond can be determined by visual inspection: bonded regions appear dark grey, while unbonded regions are much lighter. The bond is irreversible and hermetic.

NOTE: To avoid cracking of the silicon and the glass the thermal coefficients of the two must be closely matched. The linear thermal expansion coefficients of silicon and #7740 pyrex glass are $2.56 \times 10^{-6}/^{o}C$ and $3.25 \times 10^{-6}/^{o}C$, respectively.

A.3 TUBE ATTACHMENT

Figure A.4 is a section drawing (not to scale) of the bonded silicon-glass wafer with tube connector arrangements. The tube connectors are firmly attached to the glass plate, and the points of contact are leak proof.

The silicon-glass wafer was placed on a mechanical stage that can move in two directions along the horizontal plane. A tube connector (stainless steel Swagelock connector) was then held above the glass with a vice. A metal collar (stainless steel) was slipped around the

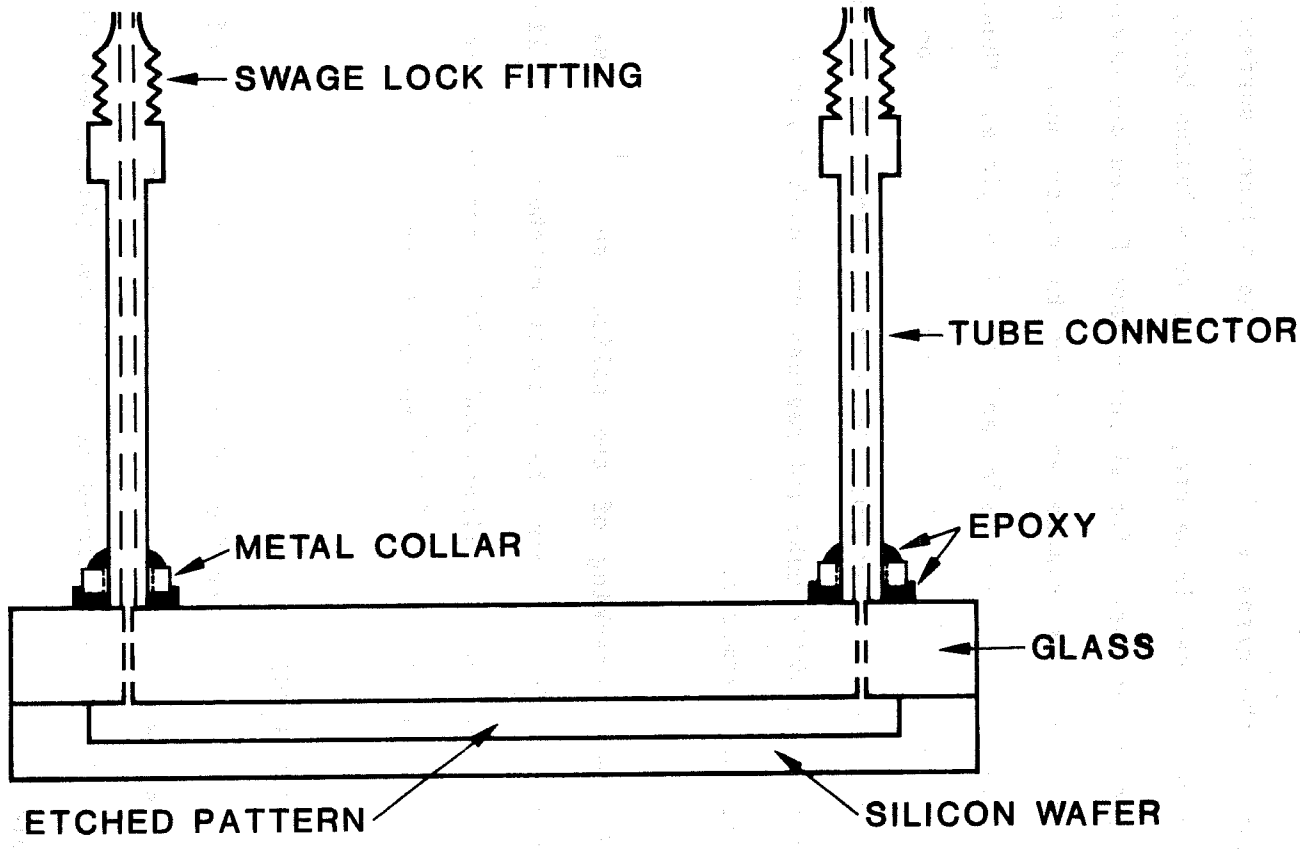

Fig. A.4 TUBE CONNECTOR ATTACHMENT

connector and held some distance above the glass and below the Swagelock threads (Fig. A.4) with a wire arrangement. The wire hangs down from the vise (not shown in the figure). By moving the vise in the vertical direction and the mechanical stage (horizontally), the tube connector was aligned over the hole in the glass. The vice was finely adjusted so that the tube barely touched the glass.

The tube was bonded to the glass with an epoxy (Eccobond 285) mixed with a catalyst (24 LV) in a proportion of 3 gm to 0.2 ml. The mixture was applied to the outer wall of the tube connector, below the metal collar. The collar was then released and allowed to slip down the connector. The collar was separated from the glass plate and the tube connector by a thin film of the epoxy. The epoxy was allowed to harden under an infrared light (heat source) for approximately two hours. Better results are obtained if the system is allowed to stand overnight after the exposure to the infrared light.

In the tube attachment, certain provisions were made to minimize the chances of damaging the model. The flowline headers must be flexible in order to reduce strain on the epoxy joints. Teflon tubings (connected to the Swagelock fittings) were used. The metal collar around the tube connector also serves as a strain relief.

The next section covers the equations governing the general fluid displacement behavior.

APPENDIX B

ANALYSIS OF FLUID FLOW IN THE MICROMODEL

The equations used in calculating absolute permeability, air flowrate, volume of air injected into the micromodel and the error in air mobility will be derived in this section.

B.1 ABSOLUTE PERMEABILITY

Figure B.1 is the fluid flow area of the micromodel. Input and output channels, (ℓ)(b), are provided on opposite ends of the porous matrix. These channels are identical in dimensions.

Fluid flow through the input and output channels in the micromodel is essentially through a slot or fracture: the channels have a width to depth ratio of approximately 70 for the homogeneous models and 420 for the heterogeneous model.

The pore spaces in the large flow area, (d)(a), interconnect and are continous from one end of the flow area to the other. This pattern constitutes a direct line drive whose wellbore radius is given by b/4. This radius (b/4) is the equivalent wellbore radius of the infinite conductivity fracture (slot) adjacent to the large flow area.

Fluid flow through the input and output channels can be represented with an equation of fluid flow through a channel. The "equivalent flow system" of the micromodel thus consists of three composite sections (flow in series): channel flow, direct line drive and channel flow.

The following equation relates the flow rate q (cc/s) to the pressure drop Δp_d (psi) across the direct line drive pattern for a fluid displacement of unit mobility ratio.

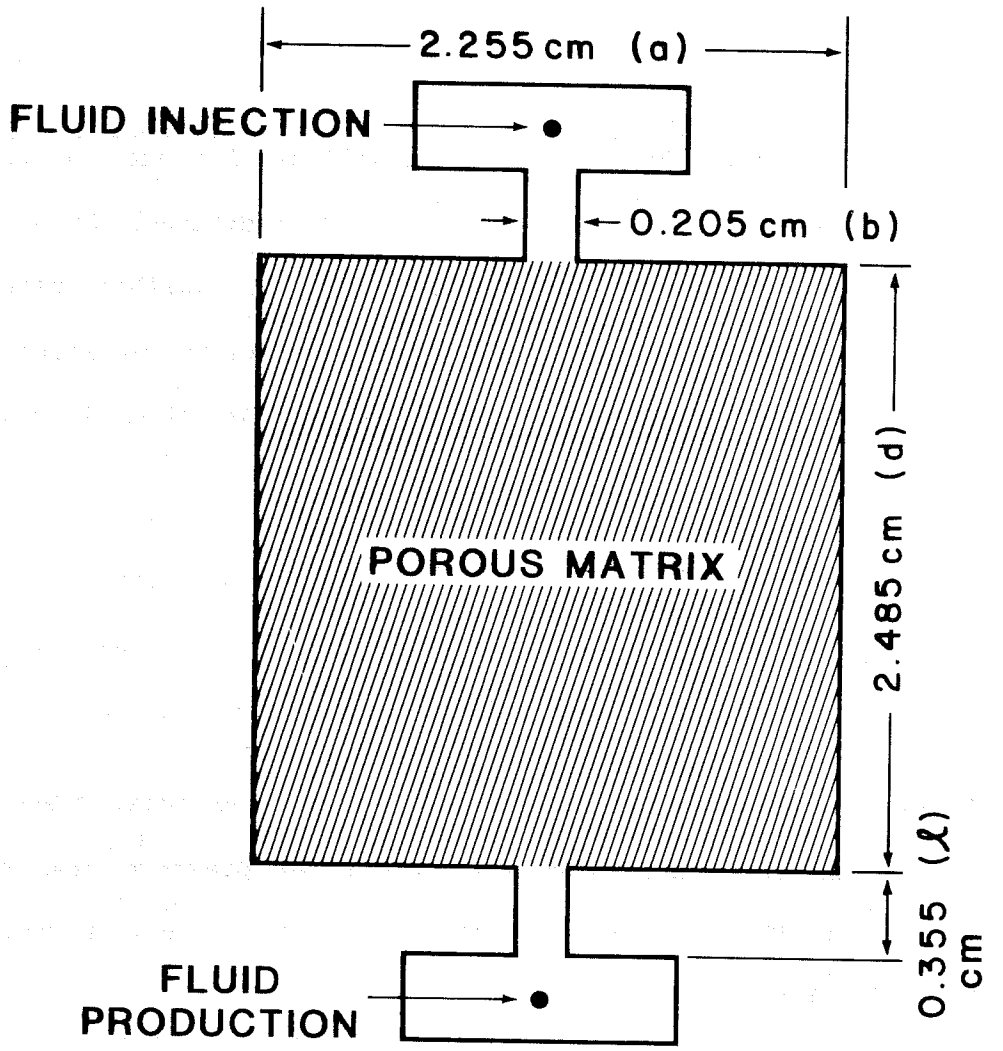

Fig. B.1 MICROMODEL FLUID FLOW SYSTEM

$$q = \frac{kh\Delta p_d}{10764\ \mu\left(\log \frac{a}{b} + 0.682\ \frac{d}{a} - 0.196\right)} \qquad (B.1)$$

The absolute permeability, k, is in millidarcies and the viscosity, μ, in centipoise. The etched depth of the micromodel is h. The other dimensions, a, b and d are shown in Fig. B.1. Wellbore radius has been replaced by b/4 in Eq. B.1. All dimensions are in centimeters.

Fluid flow through the channel (slot) is given by the following equation:

$$q = \frac{5.74\ (10^5)\ Ah^2\Delta p_f}{\mu \ell} \qquad (B.2)$$

During the experiment, the flowrate q and the total pressure drop Δp across the model are measured. The total pressure drop due to flow through the three composite sections (flow in series) is given by Eq. B.3 below:

$$\Delta p = \Delta p_d + 2\Delta p_f \qquad (B.3)$$

From equation B.1 and B.2, Δp_d and Δp_f are substituted in Eq. B.3 to obtain the following equation.

$$\Delta p = \frac{10764\mu q \left(\log \frac{a}{b} + 0.682 \frac{d}{a} - 0.196\right)}{kh} + \frac{3.484 \left(10^{-6}\right) \mu q \ell}{bh^3} \qquad (B.4)$$

Rearranging Eq. B.4, the following expression for k_d is obtained:

$$k = \frac{10764 \left(\log \frac{a}{b} + 0.682 \frac{d}{a} - 0.196\right)}{h \left(\frac{\Delta p}{\mu q} - \frac{3.484 \left(10^{-6}\right) \ell}{bh^3}\right)} \qquad (B.5)$$

B.2 AIR FLOWRATE

A syringe pump was used to inject air into the micromodel. The pump advances a syringe piston at a constant rate, and the piston displaces the air in the syringe into the micromodel. The air injection rate and flowrate in the micromodel are not constant. This is because air is compressible and the pressure in the syringe (injection pressure) is not constant. The outlet pressure is kept at atmospheric and the inlet pressure allowed to vary.

It is necessary to compute the instantaneous air flowrate and the cumulative volume of air injected. A material balance is made on the volume of air, Vs, initially in the syringe. Figure B.4 shows the syringe, the micromodel and the points where the pressures are known. The atmospheric pressure (p_a) is assumed constant throughout an

experimental run. The pressure drop, Δp, across the model is measured and the inlet pressure p is obtained by adding p_a and Δp. In this analysis, the pressure drop in the syringe will be assumed negligible. Thus, the pressure at any point in the syringe is p. The syringe includes the flow line up to the inlet pressure tap indicated in Fig. B.2.

At any time t, the number of moles of gas injected into the model plus the remaining moles of gas in the syringe equals the initial number of moles in the syringe. This material balance of the initial amount of gas in the syringe is expressed mathematically as follows:

$$\frac{p_s V_s}{Z_s R T_s} = \frac{pV}{ZRT} + \frac{pQ}{ZRT} \qquad (B.6)$$

# moles initially in the syringe		# moles remaining in the syringe	+	# moles injected into the model

p_s = initial inlet (syringe) pressure.

p = inlet pressure at time, t.

V = volume of gas remaining in the syringe.

Q = cummulative volume of air injected.

R = molar gas constant, as used only in Eq. B.6 (refer to the list of Nomenclature for the other use)

Z = gas compressibility factor.

T_s = initial temperature of the syringe.

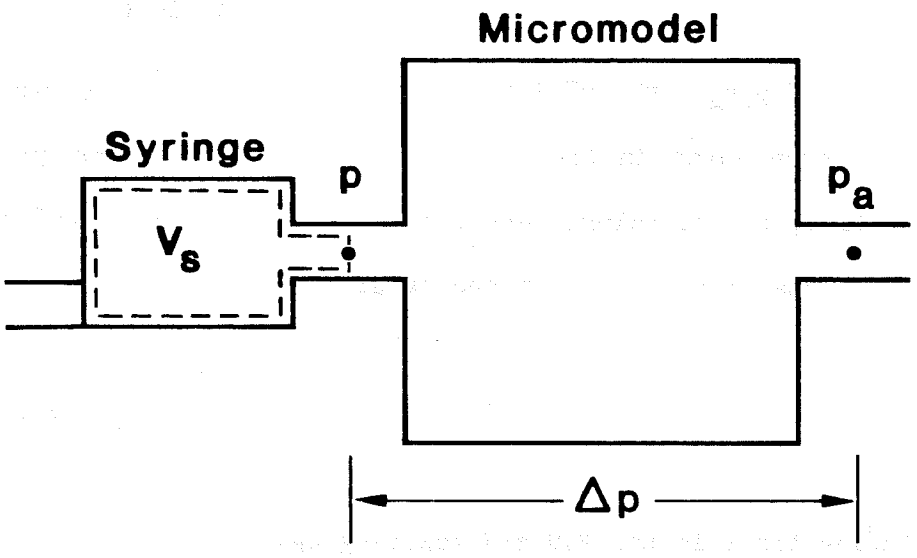

Fig. B.2 A MATERIAL BALANCE ON THE SYRINGE

T = temperature at time , t.

If the experiment is conducted at room temperature, then

$$T_s = T \qquad (B.7)$$

and

$$Z_s = Z \qquad (B.8)$$

Equation B.5 reduces to the following:

$$p_s V_s = pV + pQ \qquad (B.9)$$

The piston moves in the syringe at a constant volumetric rate, R. Thus, in time, t, the volume advanced by the piston is Rt and the volume of air, V, remaining in the syringe is given by:

$$V = V_s - Rt \qquad (B.10)$$

Substituting for V in Eq. B.9 and rearranging,

$$Qp = p_s V_s - p(V_s - Rt) \qquad (B.11)$$

Q is the cumulative volume of air injected into the model, measured at pressure p. Let Q_a represent the cumulative volume of air injected at base pressure, p_a (the atmospheric pressure) at the time of experiment. For an ideal gas:

$$Q_a = \frac{Qp}{p_a} \qquad (B.12)$$

Combining Eqs. B.11 and B.12;

$$Q_a = \frac{p_s V_s}{p_a} - \frac{p(V_s - Rt)}{p_a} \qquad (B.13)$$

but $$p = p_a + \Delta p \qquad (B.14)$$

Thus, $$Q_a = \frac{p_s V_s}{p_a} - \frac{(V_s - Rt)(p_a + \Delta p)}{p_a} \qquad (B.15)$$

The air flowrate (q_a) at time, t, is obtained by taking the derivative of Q_a in Eq. B.15, with respect to time and noting that p_s and V_s are constant for any particular run and independent of time.

$$\frac{d(Q_a)}{dt} = R + \frac{R\Delta p}{p_a} + \frac{Rt}{p_a}\frac{d(\Delta p)}{dt} - \frac{V_s}{p_a}\frac{d(\Delta p)}{dt} \qquad (B.16)$$

$$\frac{dQ_a}{dt} = q_a \qquad (B.17)$$

$$\text{Thus,} \quad q_a = R\left(1 + \frac{\Delta p}{p_a}\right) + \frac{(Rt - V_s)}{p_a} \frac{d(\Delta p)}{dt} \qquad (B.18)$$

B.3 ERROR ANALYSIS

The effective mobility of air in the presence of foam and in air-water systems were measured in the displacement experiments. The expression for the effective air mobility is given as follows:

$$\text{Effective Air Mobility (M)} = \frac{\bar{q}}{\Delta p} \qquad (B.19)$$

where $\bar{q}$ is the air flowrate in the micromodel at average pore pressure, $\bar{p}$

$$\text{Thus,} \quad \bar{q} = \frac{q_a p_a}{\bar{p}} \qquad (B.20)$$

$$\text{and} \quad M = \frac{q_a p_a}{\Delta p \, \bar{p}} \qquad (B.21)$$

Neglecting errors in p_a and $\overline{p}$, an error analysis can be made on the effective air mobility by defining the latter as follows:

$$M = \frac{q_a}{\Delta p} \qquad (B.22)$$

Substituting the expression for q_a, Eq. B.18, in Eq. B.22 one obtains the following equation for M:

$$M = \frac{R}{\Delta p} + \frac{1}{p_a} + \frac{Rt}{p_a \Delta p}\frac{d(\Delta p)}{dt} - \frac{V_s}{p_a \Delta p}\frac{d(\Delta p)}{dt} \qquad (B.23)$$

On differentiating Eq. B.23 with respect to pressure drop (Δp), time (t) and rate of change of pressure drop ($d(\Delta p)/dt$) an expression for the error for the effective air mobility is obtained:

$$d[M] = \left\{ \frac{V_s}{p_a(\Delta p)^2}\frac{d(\Delta p)}{dt} - \frac{R}{(\Delta p)^2} - \frac{Rt}{p_a(\Delta p)^2}\frac{d(\Delta p)}{dt} \right\} d[\Delta p]$$

$$+ \left\{ \frac{R}{p_a \Delta p}\frac{d(\Delta p)}{dt} \right\} d[t] + \left\{ \frac{Rt}{p_a \Delta p} - \frac{V_s}{p_a \Delta p} \right\} d\left[\frac{d(\Delta p)}{dt}\right] \qquad (B.24)$$

$d[M]$ is the error in effective air mobility.

$d[\Delta p]$ and $d[t]$ the errors in to pressure and time, respectively.

$d[\frac{d(\Delta p)}{dt}]$ is the error in the rate of change of pressure drop.

In the following section, the results from a typical experiment are presented. The method of analysis is illustrated using the data from this experiment.

APPENDIX C

EXAMPLE CALCULATIONS

Section 5 describes the calculation procedure used to obtain the effective air mobility and volume of air injected into the porous medium during the experiments. This section illustrates the procedure using data obtained from an air-water displacement experiment. The errors in the air mobility will be calculated using Eq. B.24. Table C.1 contains data needed to analyze the experimental results of Table C.2.

Table C.1

Basic Data On Example Experiment

Experiment	Air-Water Run
Date	11/24/81
Model	OW.200.48
Pore Volume, V_p, cc	0.008
Fluids	Water (distilled) and Air
Pump Rate, R, cc/s	1.28 (10^{-4})
Initial Vol. of air in Syringe, V_s, cc	1.88
Atmospheric (Room) Pressure, p_a, psia	14.8
Room temperature, T, ^oF	74
Differential Pressure Transducer Full Scale, psi	5
Initial Pressure Drop, psi	0
Time-Pressure Data	Table C.2

Table C.2 constitutes a sequence of calculations performed on the time-pressure data to obtain the pore volumes of air injected and the corresponding air mobilities. Each column of Table C.2 will now be described:

Col. 1: time, read from a timer.

Col. 2: pressure drop, measured.

Col. 3: volume of air (atmospheric) injected into the micromodel, Eq. B.15.

Col. 4: rate of change of pressure drop, numerical and graphical differentiation of time-pressure data (cols. 1 and 2).

Col. 5: air flowrate (atmospheric), Eq. B.18.

Col. 6: micromodel inlet pressure, $p_a + \Delta p$.

Col. 7: average inlet pressure, Fig. 5.2.

Col. 8: average pore pressure, Eq. 5.3.

Col. 9: p_a / Col. 8.

Col. 10: cumulative volume of air injected (at pore pressure) into the porous medium, Eq. 5.4 (trapezoid rule of integration used).

Col. 11: pore volume of air injected, Col.10 / V_p.

Col. 12: air flowrate at pore pressure, Eq. B.20, Col 10 x Col. 9.

Col. 13: effective air mobility, Eq. B.19, Col. 12 / Col. 2

Equation B.24 is used to calculate the error in the effective air mobilities of Table C.2. First the error in measuring the pressure drops and change of pressure drop with time must be known. The error in time is negligible and assumed zero. In this experiment, the error in air mobility (calculated from Eq. B.24) ranged from 20% during the first pore volume of air injection to 4% at six pore volumes. The major source of error is the calculated rate of change of pressure drop.

Table C.2

RESULTS AND ANALYSIS OF EXAMPLE EXPERIMENT

1	2	3	4	5	6	7	8	9	10	11	12	13
t, s	Δp, psi	Qa, cc	$d(\Delta p)/dt$, psi/s	q_a, cc/s	p_1, psia	$\bar{p}_1$ psia	$\bar{p}$, psia	$p_a/\bar{p}$, ratio	$\bar{Q}$, cc	$\bar{Q}/V_p$, ratio	q, cc/s	$\bar{q}/\Delta p$, cc/s/psi
1000	0.23											
1400	0.23											
1800	0.23											
2000	0.24	0.230			15.04							
2100*	0.33	0.233	$10.0(10^{-4})$	$0.220(10^{-4})$	15.13	15.08	15.08	1.000	0	0	$0.220(10^{-4})$	$0.67(10^{-4})$
2200	0.43	0.235	$10.4(10^{-4})$	$0.198(10^{-4})$	15.23	15.18	15.18	0.975	0.002	0.2	$0.193(10^{-4})$	$0.45(10^{-4})$
2400	0.63	0.240	$10.4(10^{-4})$	$0.234(10^{-4})$	15.43	15.34	15.35	0.964	0.007	0.9	$0.226(10^{-4})$	$0.36(10^{-4})$
2600	0.84	0.245	$10.4(10^{-4})$	$0.270(10^{-4})$	15.64	15.55	15.57	0.951	0.012	1.5	$0.257(10^{-4})$	$0.31(10^{-4})$
2800**	1.04	0.252	0	$1.370(10^{-4})$	15.84	15.75	15.78	0.938	0.018	2.2	$1.285(10^{-4})$	$1.23(10^{-4})$
3000	0.93	0.290	$-3.86(10^{-4})$	$1.751(10^{-4})$	15.73	15.77	15.80	0.937	0.054	6.7	$1.641(10^{-4})$	$1.76(10^{-4})$
3200	0.88	0.322	$-1.25(10^{-4})$	$1.478(10^{-4})$	15.68	15.70	15.73	0.941	0.084	10.5	$1.391(10^{-4})$	$1.58(10^{-4})$
3400	0.88	0.349	$-0.18(10^{-4})$	$1.531(10^{-4})$	15.68	15.68	15.71	0.942	0.110	13.8	$1.422(10^{-4})$	$1.64(10^{-4})$
3600	0.88	0.376	$-0.18(10^{-4})$	$1.528(10^{-4})$	15.68	15.68	15.71	0.942	0.135	16.9	$1.439(10^{-4})$	$1.64(10^{-4})$
3800	0.87	0.404	0	$1.355(10^{-4})$	15.67	15.68	15.71	0.942	0.161	20.1	$1.276(10^{-4})$	$1.47(10^{-4})$
4000	0.87	0.431	0	$1.355(10^{-4})$	15.67	15.67	15.71	0.942	0.187	23.4	$1.276(10^{-4})$	$1.47(10^{-4})$
4200	0.87											

* Air entry.

** Air breakthrough.

In the following section, a list of the equipment used for this study is presented and includes manufacturers and suppliers.

APPENDIX D

EQUIPMENT, MANUFACTURERS AND SUPPLIERS

ITEM	MODEL #	MANUFACTURER	SUPPLIERS
Syringe Pump	Sage 237-2	Sage Instruments Inc. 2 Spring Street White Plains, NY 10601	
Pressure Transducers		Celesco Transducer Prod. 7800 Deening Ave. Camga Park, CA 91305	Gado Instrument Sales 3997 E. Bayshore Road Palo Alto, CA 94566
Chart Recorder		Soltec Corporation 11684 Pendelton St. Sun Valley, CA 91352	Electronic Eng. Assoc. 932 Terminal Way San Carlos, CA 94070
Microscope	56	American Optical Scientific Inst. Div. Buffalo, NY 14215	Scientific Instrument Co. 1128 W. Evelyn Ave. Sunnyvale, CA 94086
Photographic Tube Adapter	638	"	"
Dual Viewing Adapter	270	"	"
35mm Camera Adapter	MTV-3	"	"
Video Camera	HV-62U	Hitachi	"
Video Monitor	VM-906U	"	"
Internal Coaxial Illuminator	DE-51C-99-01		"
Photo Camera	OM-2	Olympus	"
Video Recorder	VET 180	RCA	"
Micromodels	OW.200 & OW.HET		Cortnic Systems 729 Rand Ave. Oakland, CA 94610